Available online at www.sciencedirect.com

ScienceDirect

Underground Space 14 (2024) 176–196

www.keaipublishing.com/undsp

Research Paper

A simulation-based software to support the real-time operational parameters selection of tunnel boring machines

Yaman Zendaki [a], Ba Trung Cao [a,*], Abdullah Alsahly [a], Steffen Freitag [b], Günther Meschke [a]

[a] *Institute for Structural Mechanics, Ruhr University Bochum, Bochum 44801, Germany*
[b] *Institute for Structural Analysis, Karlsruhe Institute of Technology, Karlsruhe 76131, Germany*

Received 30 March 2023; received in revised form 16 June 2023; accepted 20 June 2023
Available online 14 August 2023

Abstract

With the fact that the main operational parameters of the construction process in mechanized tunneling are currently selected based on monitoring data and engineering experience without exploiting the advantages of computer methods, the focus of this work is to develop a simulation-based real-time assistant system to support the selection of operational parameters. The choice of an appropriate set of these parameters (i.e., the face support pressure, the grouting pressure, and the advance speed) during the operation of tunnel boring machines (TBM) is determined by evaluating different tunneling-induced soil-structure interactions such as the surface settlement, the associated risks on existing structures and the tunnel lining behavior. To evaluate soil-structure behavior, an advanced process-oriented numerical simulation model based on the finite cell method is utilized. To enable the real-time prediction capability of the simulation model for a practical application during the advancement of TBMs, surrogate models based on the Proper Orthogonal Decomposition and Radial Basis Functions (POD-RBF) are adopted. The proposed approach is demonstrated through several synthetic numerical examples inspired by the data of real tunnel projects. The developed methods are integrated into a user-friendly application called SMART to serve as a support platform for tunnel engineers at construction sites. Corresponding to each user adjustment of the input parameters, i.e., each TBM driving scenario, approximately two million outputs of soil-structure interactions are quickly predicted and visualized in seconds, which can provide the site engineers with a rough estimation of the impacts of the chosen scenario on structural responses of the tunnel and above ground structures.

Keywords: Numerical simulation; Surrogate model; Real-time prediction; Proper orthogonal decomposition; Radial basis functions; TBM operation; Smart construction

1 Introduction

The shield tunneling method, which employs a tunnel boring machine (TBM) for the construction process, has extensively been used for the construction of underground tunnels, especially in urban areas, due to their efficiency and smaller impact on the surrounding environment (Maidl et al., 2012). During the TBM operation, tunneling parameters must be carefully adjusted to ensure face stability, tolerated surface settlement, and improve the performance of the TBM (German Tunnelling Committee (DAUB), 2000, 2016). Within the urban area with a lot of existing buildings on the ground surface, it is essential to minimize the surface settlement, which is associated with the risks of possible damage on buildings (Cao et al., 2022). In addition, process parameters can significantly induce the deformation of the surrounding ground, which results in different pressures on the tunnel lining. In case of experiencing an intricate geological condition such as a soil layer change, applying inappropriate operational parameters may lead to exceeded settlement/heave (Suwansawat & Einstein, 2006) and damages in buildings (Selby, 1999) as well as unfavorable deformations in the tunnel lining (Zhao et al., 2021), which can cause project delay and huge compensation solutions. Therefore, in such critical

* Corresponding author.
E-mail address: ba.cao@rub.de (B.T. Cao).

https://doi.org/10.1016/j.undsp.2023.06.006

situations, it is necessary to develop an assistant tool to support the operation of TBMs to ensure the construction safety and efficiency when advancing between soil layers. The desired tool has the capability to quickly provide an accurate estimation of impacts on structural responses with respect to different possible operation scenarios. In tunneling practice, monitoring and engineering experience are commonly used to operate the TBM. Numerical simulations are mostly used for feasible and preliminary studies during the design phase rather than in the construction phase of tunneling processes. To fill in this gap, the main focus of this work is to promote the advantages of computer methods to support the TBM operation during tunnel construction by presenting a real-time assistant system based on computational simulation results. .

Up to now, computational simulation models are used only in the design phase before the actual tunnel excavation to study the feasibility of the chosen construction parameters and methods. As one of the most important soil-structure interactions in tunneling, surface settlement is considered the research object in a large number of numerical investigations. The tunneling-induced surface settlement of a large diameter shield-driven tunnel, the Yingbin San Road tunnel in China, was analyzed with a 3D finite difference (FD) model using the FLAC 3D software to optimize the construction parameters (Xie et al., 2016). A Finite Element (FE) model with detailed modeling for the excavation and steering of the TBM in case of curved alignments was presented in (Alsahly et al., 2016). More recent works focus on investigating effects on the surface settlement under critical situations such as the TBM driven under an existing historical wall (Lai et al., 2020), tunneling in saturated loess stratum (Zhu et al., 2022) and constructing overlapping tunnels in soft soils (Zheng et al., 2022). In addition, a significant number of numerical analyses pay attention not only to the settlement but also to the consequent effects on the existing buildings in urban areas. Effects of twin tunnels excavated in coarse-grained soils on the ground and structural building displacements were the focus of the work in (Fargnoli et al., 2015). In (Bilotta et al., 2017), influences of the relative position of the tunnel, the stiffness, and the weight of the building on the ground movement were studied using the data from Line 6 of Naples underground, Italy. In Miliziano & de Lillis (2019), tunneling-induced settlements and their effects on a masonry building were studied using a 3D simulation model considering the important excavation and construction processes. A similar case study, which employed a 3D model to investigate the ground movements in soft clay with and without the presence of existing historical masonry buildings, was presented in (Gong et al., 2020). Considering the 3D behavior of existing buildings due to tunneling-induced ground movement, a FE model was developed in Abaqus to perform a parametric study for a twisted building (Namazi et al., 2021). In addition to the far-field interaction (i.e., surface settlement), the effects of the tunnel construction on near-field soil-structure interactions are also reported in many works. In Do et al. (2014), a 3D numerical simulation for detailed investigations on the interaction of mechanized twin tunnels in terms of structural forces induced in the tunnel lining and ground displacement was established employing the FLAC 3D package. Recent works, which were aimed at characterizing the tunnel lining forces and ground deformations, include (Ninić & Meschke, 2017; Zhao et al., 2017; Kavvadas et al., 2017; Ochmanski et al., 2018; Do et al., 2022). In these mentioned numerical models, the soil-structure quantities were often considered solely or incompletely, e.g. either missing building damages or tunnel lining behaviors. Therefore, in order to have a multi-criteria evaluation to better support the decision-making during the shield operation, it is favorable to possess a numerical model, which can predict all the essential soil-structure interactions corresponding to a driving scenario of the TBM.

Even though simulation is a powerful tool to efficiently investigate the soil-structure interactions, the direct applicability of numerical models on real-time applications during tunnel construction is challenging due to the expensive computation time. Cheap data-driven surrogate models are thus required to substitute the time-consuming numerical model. The data used to set up surrogate models are first generated with a numerical model for a given number of possible scenarios. Similar scenarios arising from reality can then be estimated quickly by using the knowledge gained from the pre-computed simulation scenarios. Recently, numerical models used for investigations in geotechnics and tunneling have been replaced with widely-used supervised machine learning algorithms, such as support vector machine (Zhuang et al., 2019; He et al., 2020; Cheng et al., 2023), decision tree (Zhang et al., 2022), gradient boosting (Zhang et al., 2020; Bui et al., 2023), Lasso regression (Ni & Mangalathu, 2018), long short term memory (LSTM) (Guo et al., 2022), artificial neural networks (ANN) (He et al., 2020; Li et al., 2021; Ninić et al., 2017; Cao et al., 2020) for different applications, which demand fast prediction capability. Other popular methods for surrogate modeling in tunnel engineering are polynomial expansion (Majumder et al., 2017; Gan et al., 2022), response surface method (RSM) (Lü et al., 2017), Kriging (Tao et al., 2022; Zheng et al., 2023), radial basis functions (RBF) (Wang et al., 2016) and, proper orthogonal decomposition (POD) (Khaledi et al., 2014; Cao et al., 2016; Cao et al., 2018; Freitag et al., 2018). In general, these surrogate modeling approaches can work well for a prediction task with a small number of outputs (e.g., settlement at several surface points or deformations at some critical points around the lining). However, when it is required to evaluate the system response at multiple positions, in multiple time steps, or with multiple quantities, the training of prediction models may become complicated and requires a lot of effort. Among these methods, the POD and RBF methods have been successfully combined in the context of a POD-RBF surrogate model for the prediction of high-dimensional outputs with minimal

effort. In Bui et al. (2023), a POD-RBF model was utilized to predict the settlement at ten thousand surface points. Another surrogate model based on the POD-RBF approach was used in Zendaki et al. (2022) for the prediction of time evolution structural forces and deformations of lining rings, which constitutes an output vector with more than two hundred thousand values.

In this work, new contributions can be highlighted in three aspects. Firstly, an advanced 3D process-oriented simulation model based on the Finite Cell (FC) method (Bui et al., 2022) is further developed to consider all of the main soil-structure interactions within a complete simulation environment. Secondly, the efficiency of employing POD-RBF surrogate models to substitute the FC model for the prediction task with millions of output values is investigated. The high-dimensional outputs including the settlement at a large number of surface points, the strains in existing buildings, and the internal forces and deformation of the tunnel lining as well as their time evolution are then estimated in a real-time manner (i.e., in seconds). Finally, the developed strategy and related surrogate models have been packaged into a software called SMART (Simulation-and-Monitoring-based Assistant for Real-time steering in mechanized Tunneling), which can support the site engineer for the decision-making in the TBM steering phase of the construction process.

The remainder of this paper is organized as follows. Section 2 describes the concept of simulation-based TBM operation support in mechanized tunneling. Section 3 is devoted to the description of the numerical model based on the FC method. The background of the POD-RBF method, which is used as a surrogate model, is explained in Section 4. A number of application examples are presented in Section 5 to demonstrate the applicability of the proposed approach in tunneling practice. Section 6 gives a brief introduction to the assistant system SMART and manual instructions on the application of the software. Finally, conclusions and outlooks for future research are drawn in Section 7.

2 Simulation-based TBM operation concept

The concept of simulation-based TBM operation was introduced in Meschke et al. (2013), where reliable simulation results and surrogate models were employed to quickly provide accurate soil-structure interactions to support the selection of essential operational parameters (e.g., the face support pressure, the tail void grouting pressure and the advance speed) during the advancement of TBMs. To demonstrate the concept, numerical analyses were started with the consideration of the surface settlement at several monitoring points as the main soil-structure interaction in Ninić and Meschke (2015) and Zheng et al. (2023)). In Cao et al. (2016, 2018) and Freitag et al. (2015), the study was extended by considering the settlement at a large number of surface points using a hybrid combination of the POD method and Recurrent Neural Networks. A subsequent development was carried out to incorporate the surface settlement and associated damage risks on existing buildings as steering criteria to suggest appropriate applied process pressures (Cao et al., 2020, 2022). Not only the far field responses (i.e., the surface settlement and building damages) were considered in the approach, but the near field soil-structure interactions around the TBM (e.g., structural forces and deformations of the tunnel lining) were also regarded as outputs of the prognosis model (Ninić et al., 2017; Zendaki et al., 2022). In this work, all soil-structure interactions are included in the prediction model to support the TBM operation under a multi-criteria decision-making problem.

The TBM operation concept is illustrated in Fig. 1 with a specialization on a possible extreme scenario happening during the tunnel construction in an urban area, which encounters a soil layer change between two soft soil layers. In this scenario, instead of only a homogeneous soil (soil layer 1) within the complete excavated tunnel section, it is assumed that half of the tunnel section was excavated through another soil (soil layer 2). With the soil layer change, the designed steering parameters for the second half of the tunnel section are required to be adjusted to adapt to the new geological condition. For a practical application, the surrogate model would be activated only in the case of an alarm, i.e., entering another soil layer rather than the currently being excavated through. The position change between the two soil layers can be identified during tunnel construction with an automatic anomaly detection algorithm similar to the one in (Cao et al., 2021). However, the topic is out of the scope of this paper and is not discussed here.

Theoretically, numerical simulations adopting the new geological condition can be carried out to provide soil-structure interactions with respect to the new situation, however performing this task will definitely require many hours, which is not realistic for a practical application during the tunnel construction. A cheap surrogate model is then required to predict the soil-structure interactions corresponding to an arbitrary operation scenario in the new situation. To do so, firstly the surrogate model will be built based on simulation data from a number of possible operation scenarios which can be applied to the new situation. Numerical simulations using an FC model taking these scenarios as input data are then performed to generate the necessary data to set up the surrogate model. Later during the real-time application, engineers can adjust process parameters with arbitrary scenarios. Based on quick responses and evaluations of multi-output quantities, engineers have the possibility to investigate different steering possibilities before making a decision. Figure 2 presents the TBM operation concept exploiting simulation data as the basis of surrogate models for real-time prediction purposes. As an overview, in order to better support the steering decision during tunnel advance, real-time predictive simulation models will be continuously updated with monitoring data during the construction or will be combined

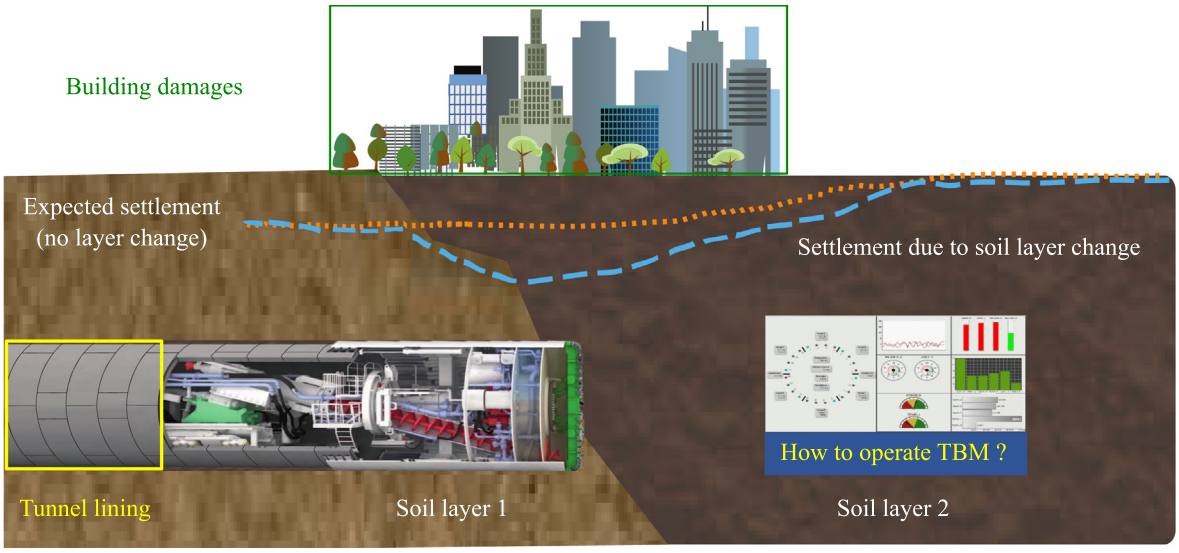

Fig. 1. TBM operation motivation: In a scenario of layer change between two soft soil layers.

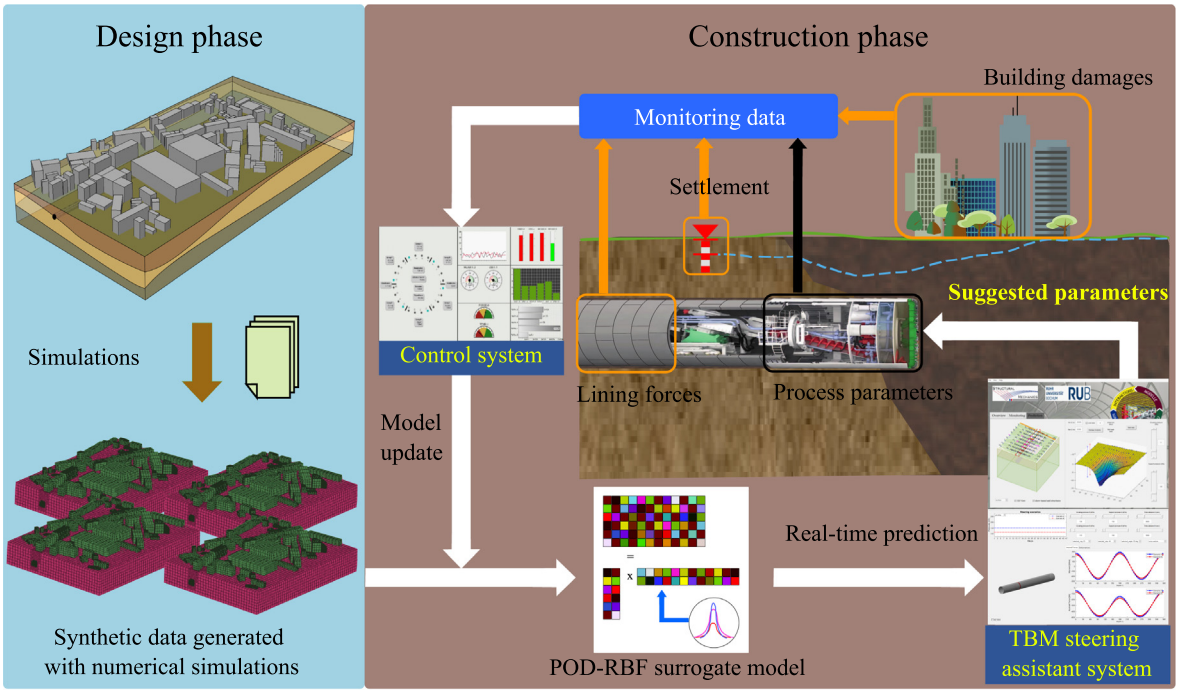

Fig. 2. The concept of simulation-based support TBM operation.

with other independent sub-models such as prediction models of logistics processes (Cao et al., 2023).

In this work, the main operational parameters taken from the literature (i.e., the face support pressure, the grouting pressure, and the advance speed during excavation) are studied numerically with respect to their sensitivities to system outputs to determine the desired inputs of the prediction surrogate model. The considered outputs are the time evolution of the settlement at multiple surface points, the time evolution of structural forces in the tunnel lining, the deformation of the tunnel lining, and the risks of damage to existing buildings.

3 Computational model for mechanized tunneling processes

In this paper, mechanized tunneling processes in soft soils are simulated using a 3D comprehensive model based on the Finite Cell method (FC) (Bui et al., 2022; Zendaki et al., 2022). The FC simulation model has recently been developed based on an advanced 3D Finite Element (FE) model (Alsahly et al., 2016; Ninić et al., 2017; Bui & Meschke, 2020; Marwan et al., 2021), which is dedicated to the simulation of TBM tunneling in soft soils. To validate the FE simulation model, data collected from either tunnel projects, such as the Wehrhahn metro line in Düssel-

dorf, Germany (Ninić et al., 2017; Bui & Meschke, 2020), or full-scale test experiments of Botlek Railway Tunnel (Marwan et al., 2021) have been used for the comparison of the simulation results with field data where it shows a good agreement between simulated and measured data. Similarly, simulated results from the FC model have been verified and compared with those produced by the validated FE model (Bui et al., 2022), which proves the validity of the FC model for the application to real-world tunneling problems. Therefore, by adopting the process-oriented FC model, soil-structure interactions during the construction of shield-driven tunnels can be simulated realistically and efficiently following a step-by-step procedure of the tunnel excavation and TBM advance. Figure 3 summarizes the validation of the FE model and the verification of the FC model using reference project data from previous works.

The main advantage of utilizing the FC method instead of the FE simulation model (Alsahly et al., 2016; Ninić et al., 2017; Cao et al., 2016) is to model components with complicated geometries and integrate them into the final tunnel model with minimal effort. In the FC approach for the simulation of tunneling processes, a simple structured background mesh is used for the soil domain, which is tied to boundary-fitted meshes representing other tunnel components such as the TBM, the tunnel lining, and the grouting, see Fig. 4(a). In this immersed boundary approach, soil layers can be modeled using a boundary representation that completely cuts through the background mesh. To account for the distribution of soil properties, geotechnical parameters of each layer are assigned to integration points, which depend on their positions with respect to each boundary representation. To enhance the accuracy and the computational efficiency of the simulation, adaptive mesh refinement (AMR) is utilized (Zendaki & Meschke, 2022), which automatically refines the structured background mesh around tunnel components and underground structures. To simulate the movement of the TBM, which is imported into the FC model as boundary-fitted mesh, an advanced steering strategy described in (Alsahly et al., 2016) or a simple algorithm to prescribe the position of the TBM in each simulation step following the desired path can be used. For more details of the FC model in the context of computational mechanics, readers are referred to the work in (Bui et al., 2022, 2023; Zendaki & Meschke, 2022).

Considering the soil–structure interaction, especially in urban areas, it is essential to appropriately incorporate existing buildings into the tunneling simulation model. Depending on the accuracy required in modeling the existing buildings, i.e., the level of details (LOD) (Ninić et al., 2019), a simple substitute model using shell elements with equivalent thickness and stiffness; 3D block volume elements; or a detailed structure with connected walls, columns, and slabs (see Fig. 4(b)) can be used to represent buildings. Figure 4(c) illustrates a model in an urban area with multiple buildings and different LODs. In general, for the simulation of a tunnel section with a large number of buildings, all buildings can be modeled using the detailed structural model, which increases dramatically the number of degrees of freedom (DOFs) of the simulation model. However, to efficiently simulate the problem, unnecessary DOFs of less important buildings are reduced using an

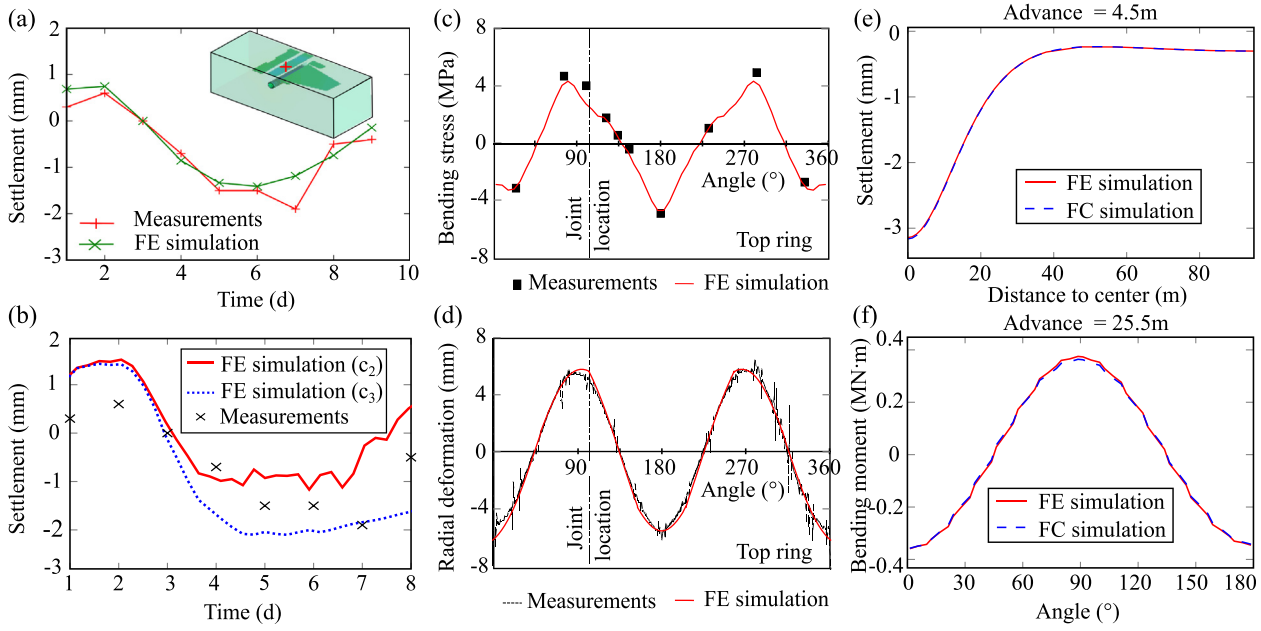

Fig. 3. Validation and verification of the simulation models (figures reproduced by the authors). (a) The settlement validation for the FE model in (Ninić et al., 2017), (b) the settlement validation for the FE model in (Bui & Meschke, 2020), (c) the bending stress validation for the FE model in (Marwan et al., 2021), (d) the lining deformation validation for the FE model in (Marwan et al., 2021), (e) the settlement verification for the FC model in (Bui et al., 2022), and (f) the bending moment verification for the FC model in (Bui et al., 2022).

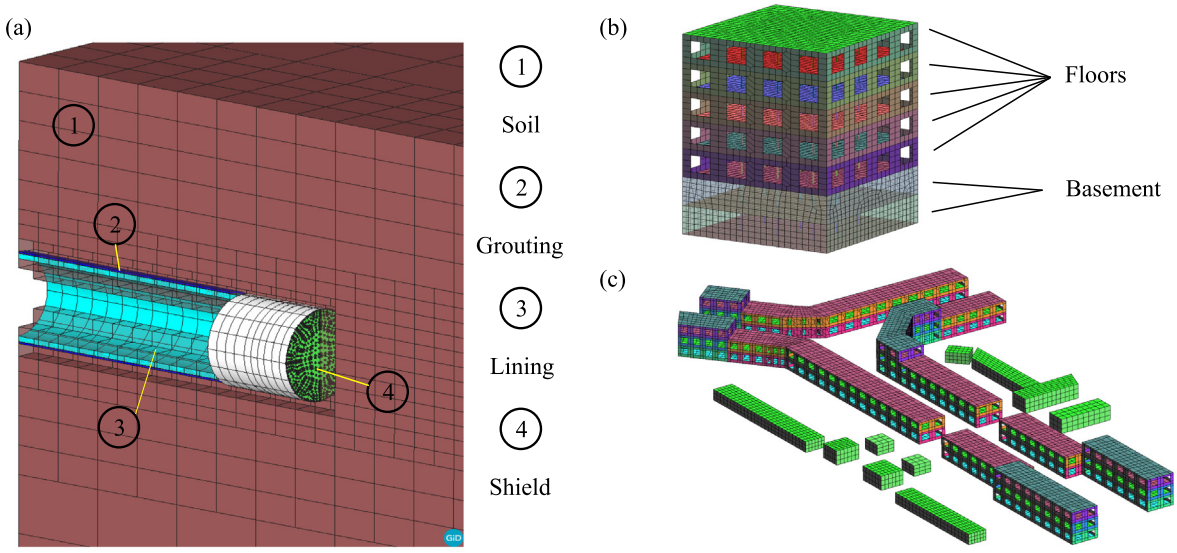

Fig. 4. Description of the FC simulation model. (a) Main components of the tunneling simulation model, (b) an example of a detailed building model, and (c) a model with multiple buildings and different LODs.

adaptive searching algorithm that assigns higher LOD to critical buildings based on their position with respect to the tunnel alignment. Whereas, less critical buildings or buildings located far away from the effective area of the tunneling process can be simulated with the lowest LOD.

Regarding the simulation of material behaviors, not only the linear elastic constitutive law is available but other advanced non-linear material models are also enabled. For example, the soil can be modeled using the well-known Mohr–Coulomb (MC) yielding criterion or clay and sand model (CASM). In the case of applying the MC model, an unloading stiffness strategy is employed to obtain a realistic behavior of the soil underneath the tunnel. The grouting elements are simulated with a time-dependent constitutive law, which takes into account the development of grouting stiffness and permeability through time from liquid to solid phases (Meschke, 1996). To better simulate damage induced by the tunneling process, buildings are modeled using shell elements and their behavior is characterized by a non-linear constitutive law, which can be used to simulate masonry or concrete structures.

4 Surrogate model for real-time prediction in mechanized tunneling

With the aim to construct an efficient surrogate model with high dimensional outputs, the Proper Orthogonal Decomposition (POD) method is combined with the well-known Radial Basis Functions (RBF). The efficiency of the POD-RBF surrogate model for predicting high dimensional outputs as compared to some popular-used machine learning models, e.g. Artificial Neural Networks or Gradient Boosting, was demonstrated in terms of accuracy and efforts for model construction in (Bui et al., 2023). Therefore, the POD-RBF method is selected to construct surrogate models for investigations in this paper. In this section, firstly the original concept of the POD method is explained, and the combination of POD and RBF to form the surrogate model for interpolation purposes is presented subsequently.

4.1 Proper orthogonal decomposition

The POD method (Smith et al., 2005) has gained popularity for applications in various fields (Everson & Sivorich, 1995; Bui-Thanh et al., 2004; Radermacher & Reese, 2014; Cao et al., 2022) due to the possibility to approximate an original high-dimensional dataset by a small-size reduced order set of basis functions with a high level of accuracy. Let us consider a collection of m snapshots of possible system solutions from numerical simulations, where each snapshot contains n output values of the FC simulation model, which correspond to a specific set of input parameters (one possible operational steering scenario), a matrix $\boldsymbol{Q}$ with n rows and m columns can be used to represent the collected data. By solving the eigenvalue problem of the sample covariance matrix $\boldsymbol{C} = \boldsymbol{Q}^{\mathrm{T}} \cdot \boldsymbol{Q}$ expressed by

$$\boldsymbol{C} \cdot \boldsymbol{V} = \boldsymbol{\Lambda} \cdot \boldsymbol{V}, \tag{1}$$

the full-order POD basis vectors $\boldsymbol{\Phi}$, which characterizes the matrix $\boldsymbol{Q}$, can be obtained. Eigenvalues and corresponding eigenvectors of the covariance matrix $\boldsymbol{C}$ are stored in the matrix $\boldsymbol{\Lambda}$ and $\boldsymbol{V}$, respectively. The approximation capabilities of the ith basis function can be estimated based on the eigenvalue λ_i (in the matrix $\boldsymbol{\Lambda}$). For the approximation of the snapshot matrix $\boldsymbol{Q}$, a desired accuracy is typically specified in order to extract only the reduced k basis functions from the full functions m ($k \ll m$). The first k POD-modes are thus denoted as truncated POD basis matrix $\hat{\boldsymbol{\Phi}}$. The snapshot matrix $\boldsymbol{Q}$ can be approximated using the

truncated basis matrix $\hat{\Phi}$ and a so-called truncated amplitude matrix $\widehat{\boldsymbol{A}}$ as

$$\boldsymbol{Q} \approx \hat{\Phi} \cdot \widehat{\boldsymbol{A}} \ . \tag{2}$$

At this step, the truncated amplitude matrix $\widehat{\boldsymbol{A}}$ is computed as

$$\widehat{\boldsymbol{A}} = \hat{\Phi}^{\mathrm{T}} \cdot \boldsymbol{Q}. \tag{3}$$

4.2 Proper orthogonal decomposition and radial basis functions

In Eq. (3), only information of steering scenarios used to create the snapshots is stored in the matrix $\widehat{\boldsymbol{A}}$. To predict the output of arbitrary steering scenarios, which are not included in the snapshot matrix, the matrix $\widehat{\boldsymbol{A}}$ is reformulated to become a smooth interpolation function of input parameters. Given the collection of input scenarios snapshots stored in the matrix $\boldsymbol{Z}$, the distances or mutual relations between a scenario and other scenarios in the snapshots are described using a set of vectors $\boldsymbol{F}^i$ $(i = 1 \cdots m)$ as follows

$$\boldsymbol{F}^i = \left[f_1(\boldsymbol{Z}^i) \cdots f_j(\boldsymbol{Z}^i) \cdots f_m(\boldsymbol{Z}^i)\right]^{\mathrm{T}}, \tag{4}$$

with $f_j(\boldsymbol{Z}^i)$ are predefined interpolation functions of the input scenario $\boldsymbol{Z}^i$ $(j = 1 \cdots m)$. Each amplitude vector $\widehat{\boldsymbol{A}}^i$ is then defined as a linear combination of $\boldsymbol{F}^i$ and an unknown coefficient matrix $\boldsymbol{B}$ as

$$\widehat{\boldsymbol{A}}^i = \boldsymbol{B} \cdot \boldsymbol{F}^i. \tag{5}$$

For the interpolation function, the inverse multi-quadric radial basis function (RBF) (Hardy, 1990; Buhmann, 2003) is adopted in this paper due to the good approximation and smoothing properties. Therefore, each element of the vector $\boldsymbol{F}^i$ is defined as

$$f_j(\boldsymbol{Z}^i) = f_j(|\boldsymbol{Z}^i - \boldsymbol{Z}^j|) = \frac{1}{\sqrt{|\boldsymbol{Z}^i - \boldsymbol{Z}^j|^2 + c^2}}, \tag{6}$$

where c is called the smoothing factor selected based on the shape parameter β and the distance d^i between the ith data point and its neighbor according to (Hardy, 1990). Being formed from all vectors $\boldsymbol{F}^i$ of input parameters used to generate the snapshots, the matrix $\boldsymbol{F}$ is then used to compute the *truncated* amplitude matrix $\widehat{\boldsymbol{A}}$ as

$$\widehat{\boldsymbol{A}} = \boldsymbol{B} \cdot \boldsymbol{F}. \tag{7}$$

The coefficient matrix $\boldsymbol{B}$ is determined from Eqs. (3) and (7). Finally, an approximation of the output system response (soil-structure interaction quantities) $\boldsymbol{Q}^{\mathrm{a}}$ corresponding to an arbitrary set of inputs (an operational steering scenario) $\boldsymbol{Z}^{\mathrm{a}}$ is obtained by

$$\boldsymbol{Q}^{\mathrm{a}} \approx \hat{\Phi} \cdot \boldsymbol{B} \cdot \boldsymbol{F}^{\mathrm{a}}. \tag{8}$$

For a more comprehensive description and step-by-step algorithms of the POD and POD-RBF procedures, readers are referred to (Cao et al., 2016; Freitag et al., 2018).

5 Application examples

This section is devoted to an application of the proposed concept for the simulation-supported real-time TBM operation based on two synthetic examples. In the first example, the steering scenarios are investigated within a section with no buildings on the top ground surface, i.e., green-field settlements. Parametric studies are first carried out in order to determine the sensitivity of input parameters (i.e., steering parameters) to numerical outputs (i.e., the expected soil-structure interaction outputs). The design of possible steering scenarios is then illustrated in more detail. As the next step, the creation and the quality evaluation of the POD-RBF surrogate model are presented using the simulation results. To assess the prediction quality of the surrogate model, the predicted results for test data sets are compared with reference solutions from FC simulations. The workflow of the presented strategy is summarized in Fig. 5.

In the second example, an extension of the first example is investigated following the same procedure but considering a scenario for tunnel construction support in an urban area, where it is necessary to assess the risk of damages in existing buildings with respect to the variations of a steering scenario due to a soil layer change in geological condition. For this purpose, a synthetic example, which is inspired by the geometry of a tunnel section with lots of buildings from a real reference tunnel project, is created in the second example.

5.1 TBM process control in green field settlement area

In this example, a tunnel model of 114 m with the excavation diameter of $D = 7.81$ m constructed by a TBM is generated, see Fig. 6, using the FC model described in Section 3. The simulated model with no building on the top ground surface represents a tunnel section with green-field settlement. The tunnel is excavated with an overburden of 11 m, i.e., the ratio between the cover depth and the tunnel diameter D is approximately 1.4. Dimensions of the model in Y and Z directions, which are chosen with the consideration of avoiding boundary effects on the results of numerical analysis, are 273 and 56 m, respectively. The tunnel lining is modeled as a continuous ring, which is made of concrete with a length of 1.5 m and a thickness of each lining ring of 0.45 m. The material behavior of the lining ring and the shield machine is assumed to be linear elastic with the moduli of elasticity of 30 and 210 GPa, respectively. The grouting elements are modeled with a time-dependent development of stiffness with the final modulus of elasticity of 5 GPa. Regarding the boundary conditions, horizontal displacements of surrounding surfaces of the simulation domain are restrained. To the extent that there is hardly any deformation in deeper soil

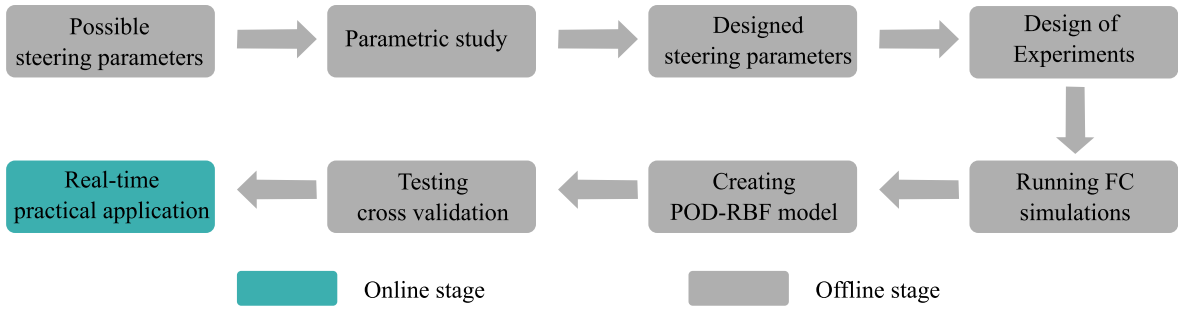

Fig. 5. Flow chart of the presented simulation-supported real-time TBM operation strategy.

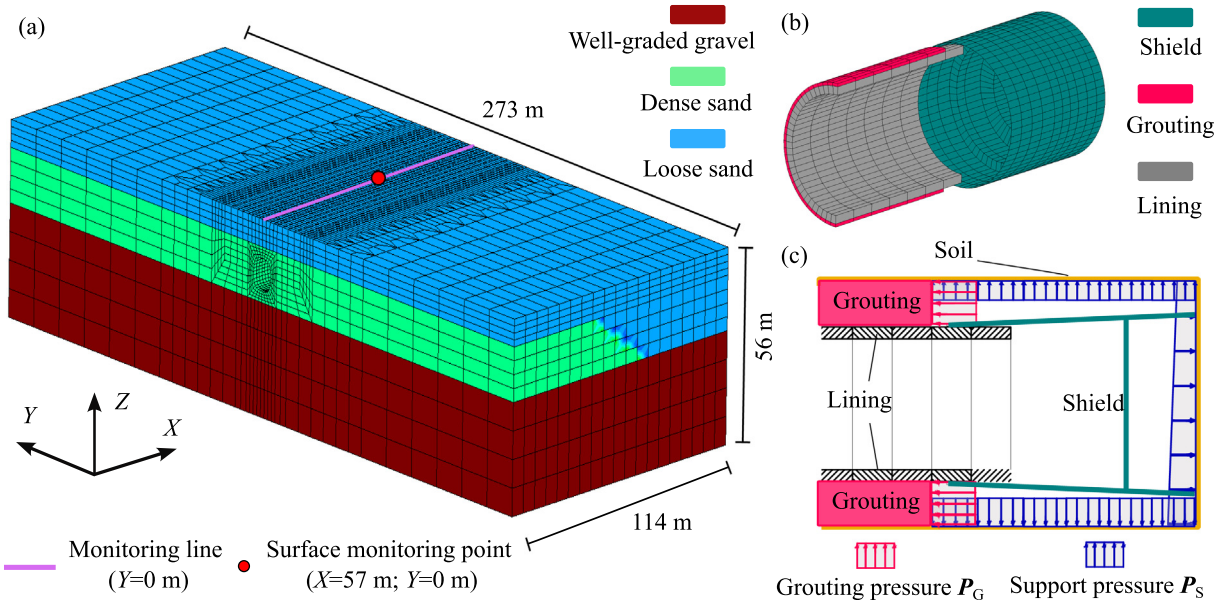

Fig. 6. Simulation model of the tunnel section with green field settlement. (a) Model overview, (b) lining, grouting & TBM model, and (c) boundary conditions representing the applied P_S and P_G.

layers with high stiffness, the bottom boundary is completely fixed in both horizontal and vertical directions as typically used in applications of the numerical methods to geotechnical problems. The model consists of 59 384 elements and 228 643 degrees of freedom, which represents the tunnel section with 76 rings or excavation slices. Due to the fact that the excavation process of the first 5 rings and the last 9 rings of the model are not taken into account for avoiding boundary conditions effects, a total number of 62 excavation steps are simulated in each simulation.

It is assumed that the ground model is taken from the geotechnical report as shown in Fig. 7 comprising three soil layers: a loose sand layer, a dense sand layer (approximately 15 m thick) and a well-graded gravel layer (approximately 33 m thick). The thickness of the loose sand layer is approximately between 8 to 23 m due to a soil layer change existing between ring 28 and ring 48, i.e., at the middle of the tunnel section, see Fig. 7. As a result, within the first half of the tunnel section, the tunnel is excavated in the dense sand layer, whereas in the second half of the domain section, the tunnel is actually constructed in a softer soil layer, i.e., the loose sand layer. Therefore, after detecting the soil layer change during the tunnel construction, a new steering scenario, which is adapted to the new geological situation, needs to be carried out. To simulate the behavior of soil layers, an elastoplastic model using the Mohr–Coulomb yield criterion is employed in this paper. The design material parameters (density γ, modulus of elasticity E, Poisson's ratio ν, and internal friction angle ϕ) of the soil layers are shown in Fig. 7.

With respect to operational process parameters, three main parameters: the support pressure P_S and the grouting pressure P_G together with the advance speed V_S of the TBM, are selected. The first two pressures are applied at the tunnel heading face and tail void gap respectively, while the advance speed V_S represents the time of both soil excavation and lining ring assembly. Regarding the soil layer change, it is also interesting to investigate the effects on soil-structure interactions, when the new steering scenario is applied during the excavation of the soft soil layer. In other words, the influence of "on time" or "too late" applying the new steering scenario is investigated. This parame-

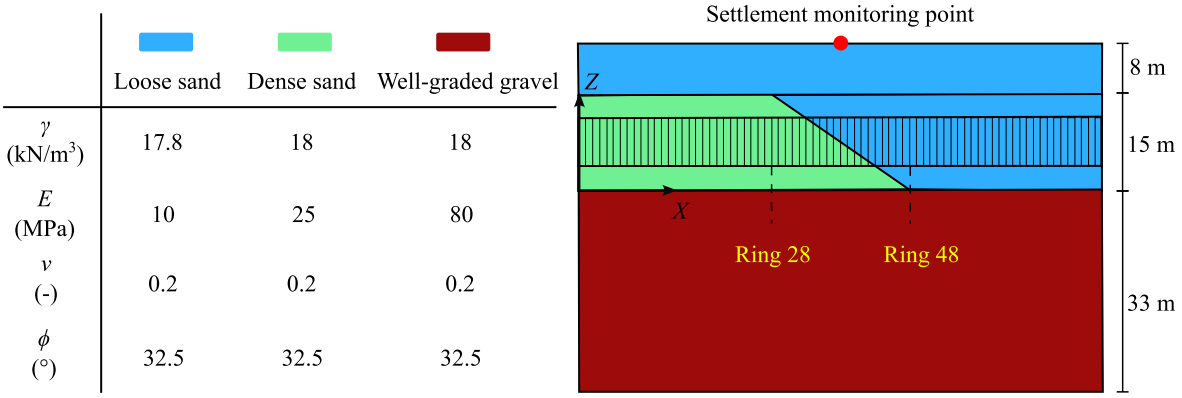

Fig. 7. Geological conditions of the simulated tunnel section.

ter is called steering time and denoted as $\boldsymbol{T}_S$. The sensitivity of these process parameters to the outputs (e.g., surface settlement $\boldsymbol{S}$, bending moments $\boldsymbol{M}$, and normal forces $\boldsymbol{N}$ in the tunnel lining) are investigated within the scope of a parametric study to select appropriate input parameters of the surrogate model.

5.1.1 Parametric study of operational process parameters

Before defining the design of experiment to generate simulation samples for the creation of the surrogate models, a brief parametric study is performed by running a number of simulations with different steering parameters to roughly estimate their effects on the expected soil-structure interactions simulation results. The steering parameters are varied only during the excavation of the softer soil layer, i.e., varying $\boldsymbol{P}_S^2$ and $\boldsymbol{P}_G^2$, while the applied parameters for the tunnel section in the stiff soil layer ($\boldsymbol{P}_S^1$ and $\boldsymbol{P}_G^1$) are kept consistent for all simulations in the parametric study. The less sensitive parameters will not be considered as the inputs of the surrogate model since even a big change in the input parameters will lead to similar results in the outputs. Only parameters with high sensitivities will be considered as inputs of the surrogate model.

More specifically, six simulations (Case A to Case F) defined in Table 1 representing possible applied ranges of the four investigated parameters ($\boldsymbol{P}_S, \boldsymbol{P}_G, \boldsymbol{V}_S$ and $\boldsymbol{T}_S$) are executed and the simulated results are extracted and visualized in Figs. 8 and 9. The applied values of steering parameters in the six simulations are summarized in Table 1. It

Table 1
Applied values of selected steering/operational parameters in the parametric study.

	$\boldsymbol{P}_S^1$ (kPa)	$\boldsymbol{P}_S^2$ (kPa)	$\boldsymbol{P}_G^1$ (kPa)	$\boldsymbol{P}_G^2$ (kPa)	$\boldsymbol{V}_S$ (s/ring)	$\boldsymbol{T}_S$ (Ring No.)
Case A	140	180	140	180	5400	38
Case B	140	140	140	180	5400	38
Case C	140	140	140	140	5400	38
Case D	140	140	140	140	9000	38
Case E	140	180	140	180	5400	28
Case F	140	180	140	180	5400	48

should be noted that the applied ranges are taken considering the practical tunneling guidelines, e.g., the applied $\boldsymbol{P}_S$ should be greater than a minimum value to guarantee the tunnel face stability and should not exceed a certain value to avoid the blowout phenomenon. To illustrate the effects of $\boldsymbol{P}_S$, model responses in two scenarios (Case A & Case B) are compared, whereas the sensitivities of other steering parameters to soil-structure interactions can be analyzed in comparisons between Case B & Case C for $\boldsymbol{P}_G$, and between Case C & Case D for $\boldsymbol{V}_S$. In this example, the transition zone between the stiff soil layer and the softer soil layer is assumed between ring 28 and ring 48, see Fig. 7. As a result, three simulations (Case A, Case E & Case F) investigate the adjustment of the steering time $\boldsymbol{T}_S$ corresponding to three TBM locations: at ring No. 28 (Case E) when the TBM is entering the new softer layer, ring No. 38 (Case A) when the TBM is in the middle of the transition zone and ring No. 48 (Case F) when the TBM is passing completely the zone. In addition, in each pair of simulations, all model parameters remain unchanged except for the varied parameter. It should be mentioned that the inclination of the soft layer is assumed to be fixed and is thus not considered in the parametric study.

Effects of operational parameters on the settlement are shown in Fig. 8. Figure 8(a) presents the time evolution settlements of a monitoring surface point located at a distance of 57 m from section boundary in X direction, i.e., the red point in Fig. 6(a), with respect to the four simulations (Case A to Case D). The longitudinal displacements at the final simulation step of a top surface line (the purple line in Fig. 6(a)) under these four scenarios are plotted in Fig. 8(c). To compare the responses with different $\boldsymbol{T}_S$, which corresponds to three scenarios (Case A, Case E & Case F), the time evolution settlements and the longitudinal displacements are visualized in Fig. 8(b) and (d), respectively.

The results in Fig. 8(a) and (c) clearly illustrate that the differences in $\boldsymbol{P}_S$ (between Case A & Case B) and in $\boldsymbol{P}_G$ (Case B & Case C) have significant influences on $\boldsymbol{S}$. Among them, the sensitivity of $\boldsymbol{P}_S$ to $\boldsymbol{S}$ is higher than the sensitivity of $\boldsymbol{P}_G$ in these applied ranges. On the other hand, the sur-

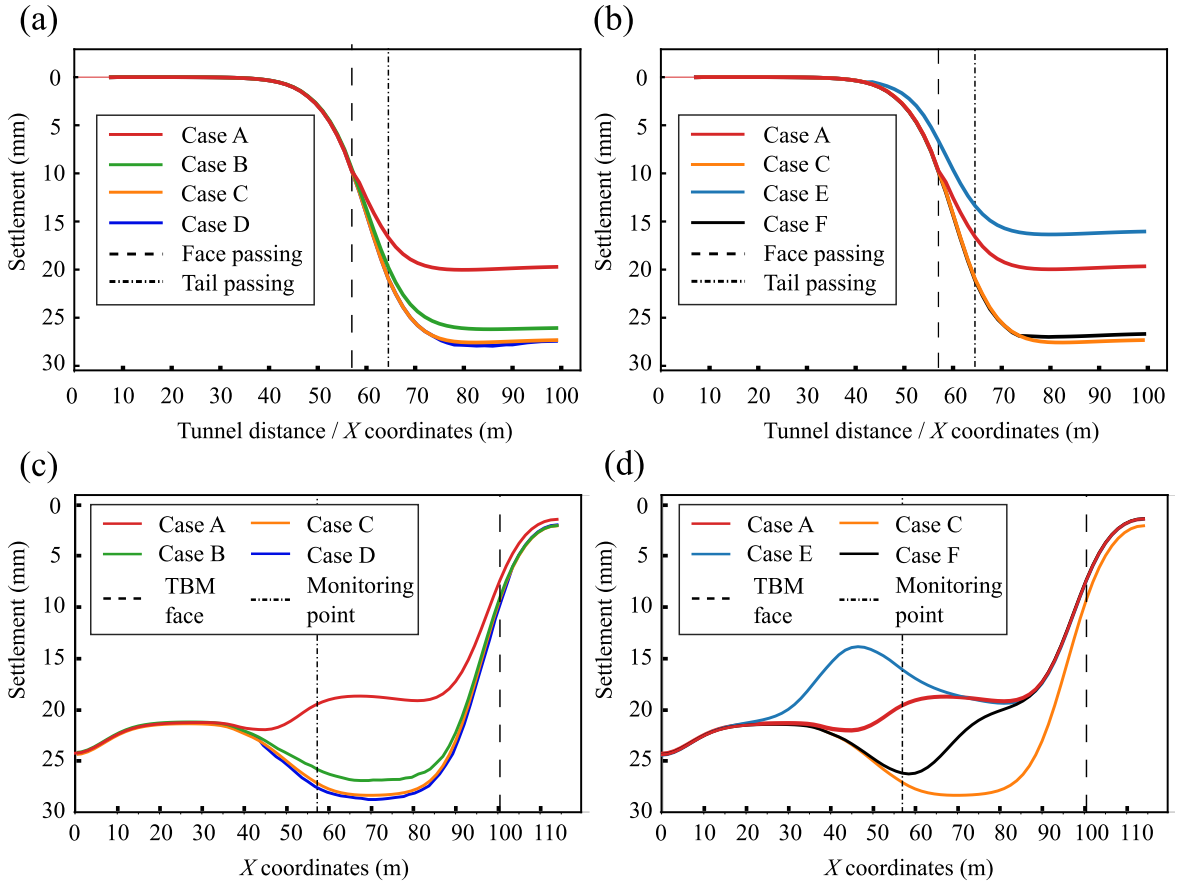

Fig. 8. Parametric study of operational parameters effects on settlements. (a) Effects of $\boldsymbol{P}_S$, $\boldsymbol{P}_G$ & $\boldsymbol{V}_S$ on evolution settlements of a surface point ($X = 57$ m, $Y = 0$ m), (b) effects of $\boldsymbol{T}_S$ on evolution settlements of a surface point ($X = 57$ m, $Y = 0$ m), (c) effects of $\boldsymbol{P}_S$, $\boldsymbol{P}_G$ & $\boldsymbol{V}_S$ on the longitudinal displacement of a surface line ($Y = 0$ m), and (d) effects of $\boldsymbol{T}_S$ on the longitudinal displacement of a surface line ($Y = 0$ m).

face settlements are not sensitive to the variation of time advance speed $\boldsymbol{V}_S$, as clearly shown in Figs. 8(a) and (c) in a comparison between Case C & Case D. Even though a wide range of $\boldsymbol{V}_S$ is used, the difference in $\boldsymbol{S}$ is almost negligible. The importance of the soil layer change detection problem can be well recognized from the investigation results in Fig. 8(b) and (d). The earlier the soil layer change (e.g., in Case E) is detected and the steering scenario is adapted, the better settlement can be controlled or minimized. If the adjustment is performed too late such as in Case F, when the TBM is completely in the new softer soil layer, the settlement of the critical monitoring point can be hardly controlled. Even applying a steering scenario with high values of $\boldsymbol{P}_S^2 = 180$ kPa and $\boldsymbol{P}_G^2 = 180$ kPa, the development curve of the settlement in Case F, see Fig. 8(b), is almost the same as the curve of the unchanged steering scenario (i.e., Case C).

Figure 9 is devoted to the demonstration of the lining responses with different steering scenarios. The time evolution of $\boldsymbol{M}$ of the ring 39 at the monitoring angle 0° is compared in Fig. 9(a). Whereas, Fig. 9(c) depicts the respective time evolution of $\boldsymbol{N}$. Effects of $\boldsymbol{T}_S$ on $\boldsymbol{M}$ and $\boldsymbol{N}$ are illustrated in Fig. 9(b) and (d), respectively. The same trend can be well concluded in Fig. 9(a) and (c) with respect to the effects of $\boldsymbol{P}_S, \boldsymbol{P}_G$ and $\boldsymbol{V}_S$ on the lining forces (i.e., $\boldsymbol{M}$ and $\boldsymbol{N}$). The pressure $\boldsymbol{P}_S$ is the most sensitive parameter to the lining forces, while slight changes in the structural forces of the tunnel lining can be achieved by varying $\boldsymbol{P}_G$. Similar to the finding related to the settlement, the sensitivity of $\boldsymbol{V}_S$ to $\boldsymbol{M}$ and $\boldsymbol{N}$ is also insignificant. This means that the variability of $\boldsymbol{V}_S$ is not sensitive to the simulated soil-structure interactions, whereas Fig. 9(b) and (d) show substantial variations on the lining forces with different $\boldsymbol{T}_S$. Therefore, together with $\boldsymbol{P}_S$ and $\boldsymbol{P}_G$, steering time $\boldsymbol{T}_S$ will be considered as inputs, while $\boldsymbol{V}_S$ is excluded from the inputs of the surrogate model in the construction support strategy in this paper.

5.1.2 Steering scenarios creation for the Design of Experiments

In order to design possible steering scenarios, combinations of the operational steering parameters (i.e., $\boldsymbol{P}_S$ and $\boldsymbol{P}_G$) are carried out with the consideration of their mutual constraints following practical tunneling guidelines. More specifically, based on the overburden and soil properties, the applied $\boldsymbol{P}_S$ is determined using the suggestions from construction guidelines. However, the actual applied value can be adjusted around the suggested value but still need to

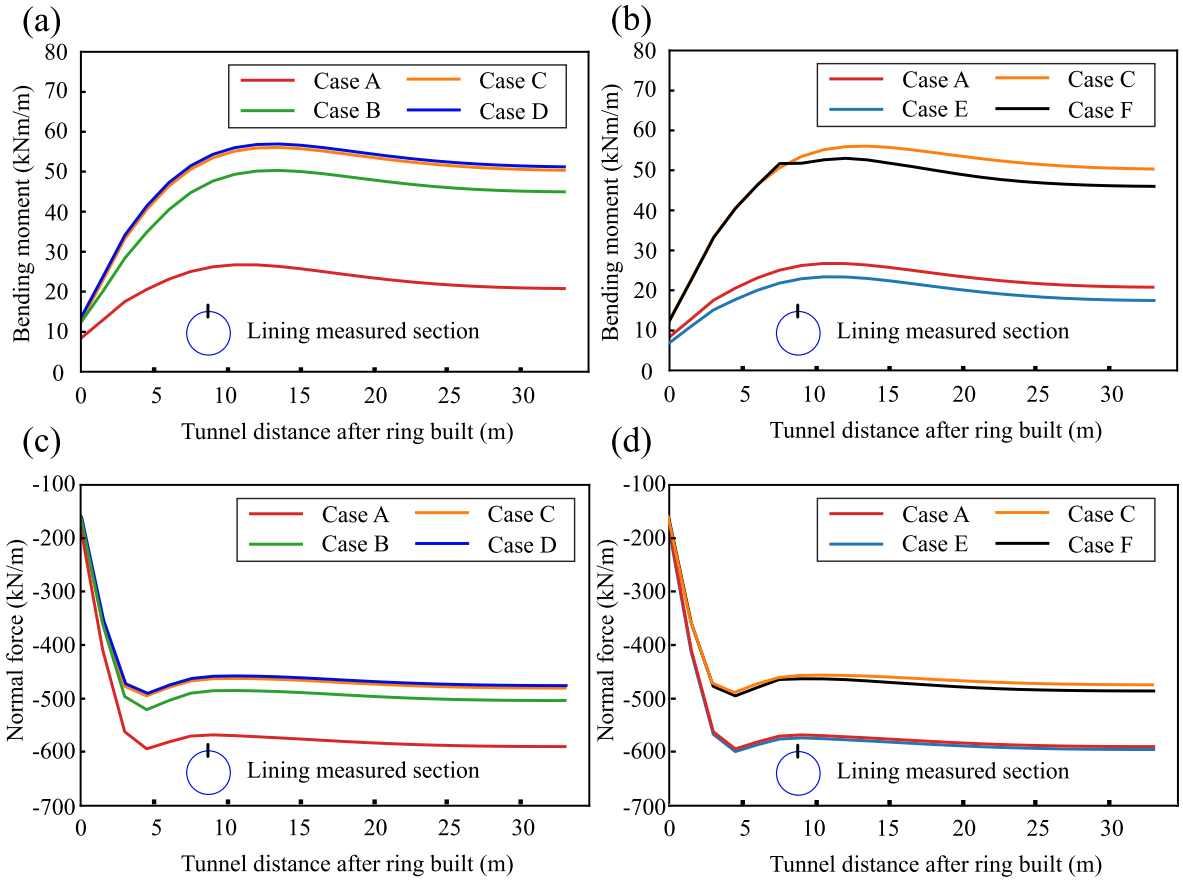

Fig. 9. Parametric study of operational parameters effects on lining responses. (a) Effects of $\boldsymbol{P}_S, \boldsymbol{P}_G$ & $\boldsymbol{V}_S$ on the bending moments of lining ring 39 at section angle 0°, (b) effects of $\boldsymbol{T}_S$ on the bending moments of lining ring 39 at section angle 0°, (c) effects of $\boldsymbol{P}_S, \boldsymbol{P}_G$ & $\boldsymbol{V}_S$ on the normal forces of lining ring 39 at section angle 0°, and (d) effects of $\boldsymbol{T}_S$ on the normal forces of lining ring 39 at section angle 0°.

satisfy certain criteria, such as being greater than a minimum value to guarantee the tunnel face stability and not exceeding a certain value to avoid the blowout phenomenon. Similarly, $\boldsymbol{P}_G$ is set slightly higher than $\boldsymbol{P}_S$ as done in practice to guarantee that the grout will fill the space between the lining and the soil.

In this example, the suggested $\boldsymbol{P}_S$ is 140 kPa depending on the depth, the soil properties, and the water pressure, which is 120 kPa at this depth. The possible applied ranges of $\boldsymbol{P}_S$ are determined from 100 to 180 kPa. Eight values in the applied ranges $[100 \cdots 180]$ kPa are discretized to define eight possible applying face pressure scenarios. The eight input values are selected based on a preliminary study that aims at defining the input discretization to well represent the range of settlement outputs. Considering the applying of face pressure in the dense sand layer ($\boldsymbol{P}_S^1$) and the loose sand layer ($\boldsymbol{P}_S^2$), there are thus sixty-four scenarios of applying $\boldsymbol{P}_S$ in the tunnel section. The $\boldsymbol{P}_G$ is varied based on the applied $\boldsymbol{P}_S$ with three levels of changing magnitudes $l = [0, 1, 2]$ as follows

$$\boldsymbol{P}_G = \boldsymbol{P}_S + l \cdot \Delta \boldsymbol{P}_G, \tag{9}$$

where $\Delta \boldsymbol{P}_G = 10$ kPa represents the relative amount of changing in $\boldsymbol{P}_G$. In other words, corresponding to a scenario of $\boldsymbol{P}_S$, there are nine possibilities to apply $\boldsymbol{P}_G$ (three for the $\boldsymbol{P}_S^1$ in the dense sand layer and three for the $\boldsymbol{P}_S^2$ in the softer soil layer), which leads to a set of 576 scenarios of applying both operational parameters $\boldsymbol{P}_S$ and $\boldsymbol{P}_G$ in the tunnel section. To react to the soil layer change problem, five steering times $\boldsymbol{T}_S$ (at ring 28, ring 33, ring 38, ring 43, and ring 48) are selected to start adjusting the operational parameters.

A total number of 2880 scenarios, which will be simulated using the FC model, are designed for this example, see Table 2. Finally, if encountering a soil layer change problem, engineers can quickly answer the questions: how much the operational steering parameters ($\boldsymbol{P}_S$ and $\boldsymbol{P}_G$) should be adjusted and when the adjustment should be made, inside the transition zone between two layers or later completely in the new soil layer.

5.1.3 Surrogate model training and testing

In this application example, the quantities of interest are: (1) the time evolution settlement $\boldsymbol{S}$ at 2457 surface points, which are taken from the structured mesh of the FC simulation model; (2) the time evolution lining forces ($\boldsymbol{M}, \boldsymbol{N}$ and $\boldsymbol{L}$) and displacements ($\boldsymbol{u}_x, \boldsymbol{u}_y$ and $\boldsymbol{u}_z$) in all 76 rings of the tunnel section. As mentioned earlier, the time

Table 2
Design of experiments for the green field settlement example.

	Stiff soil	Softer soil	No. of samples
Support pressure	$\boldsymbol{P}_S^1 = [100 \cdots 180]$	$\boldsymbol{P}_S^2 = [100 \cdots 180]$	64
Grouting pressure	$l_1 = [0, 1, 2]$	$l_2 = [0, 1, 2]$	9
Steering time	$\boldsymbol{T}_S = [28, 33, 38, 43, 48]$		5
Total			**2880**

evolution in each simulation consists of 62 simulation steps, while the circular lining ring is represented by 64 points uniformly located every 5.625° around the lining. Seven POD-RBF models (Model 1 to Model 7) are constructed to predict each quantity individually. The respective size of the output vector of each quantity is presented in Table 3, which emphasizes the necessity for a prediction surrogate model with a high dimensional output. It is worth mentioning that in a real-time application, corresponding to each new input steering scenario, the seven models are called and quickly provide the predicted soil-structure interactions under the output vector/matrix type. The results are then re-organized and visualized in an engineering-oriented way such as 3D surface settlement plots, 3D lining deformation plots, or time evolution settlement graphs.

To evaluate the quality of POD-RBF models, 5-fold cross-validation is used. From the 2880 simulations, 5 sub data sets with equal size are split to perform the 5-fold cross-validation. Figure 10 illustrates the data split for the test set within the cross-validation procedure for the prediction of surface settlement. The data is split to guarantee that number of samples in the test set of each fold corresponding to all $\boldsymbol{T}_S$ groups are similar. Otherwise, if a prediction model is trained based on the data of a specific $\boldsymbol{T}_S$, it is not possible to predict the system behavior with respect to another steering time $\boldsymbol{T}_S$. In each validation, the prediction quality of POD-RBF models is evaluated by comparing the predicted $\boldsymbol{Q}^*$ and the "true" FC reference results $\boldsymbol{Q}^{FC}$ using the well-known coefficient of determination R^2 and the L_2 norm error, which is defined as

$$\|e\|_{L_2} = \sqrt{\frac{\sum_{i=1}^{os}\left(\boldsymbol{Q}_i^{FC} - \boldsymbol{Q}_i^*\right)^2}{\sum_{i=1}^{os}\left(\boldsymbol{Q}_i^{FC}\right)^2}} \times 100\%, \tag{10}$$

where os is the output size of the vector $\boldsymbol{Q}^*$. The mean R^2 values and L_2 norm errors of all validation cases in each fold, including the average error of the 5-fold cross-validation are given in Table 4. The histogram of L_2 prediction errors from all 2880 scenarios for all quantities of interest is illustrated in Fig. 11. As observed, prediction errors of several cases are approximately 7% or 8% (e.g., for the prediction of lining deformations $\boldsymbol{u}_x, \boldsymbol{u}_z$ or shear force $\boldsymbol{L}$), however overall there are no scenarios exceeding the error tolerance of 10%, which is normally acceptable for practical applications in various engineering fields. Additionally, with the distribution of L_2 norm errors mainly within the range from 1% to 3% and the overall R^2 value of 0.999, all the POD-RBF models show an excellent generalized prediction capability.

To give a better illustration of the prediction quality in an engineering-oriented manner, among the 2880 available simulation cases, the worst prediction performances of the POD-RBF model related to the surface settlement at the excavation step 55 is selected for visualization, see Fig. 12 (a) and (b). Whereas Fig. 12(c) is dedicated to presenting the worst prediction related to lining deformations $\boldsymbol{u}_z$ of the ring 40 at simulation step 55. Even for the worst-case scenarios (with an error of 3.9% for the settlement prediction and an error of 5.6% for the lining deformation $\boldsymbol{u}_z$ prediction), one can see a very good level of prediction of the POD-RBF model for both the surface settlement and the lining deformation. Certainly, for most scenarios, where errors are between 1% and 3%, the prediction results look even more precise and identical to the FC solutions.

With an average L_2 norm error of approximately 1.4% and R^2 value of 0.999 with almost two million output elements and a generalized robust prediction capability, it can be concluded that the POD-RBF surrogate models are able to produce appropriate prediction results with similar accuracy as compared to the FC solutions. Regarding the computation time, using the trained surrogate models instead of an FC simulation leads to a substantial reduction from 7 h to around 5 to 10 s in order to predict the almost two million outputs for a tunneling scenario, which

Table 3
Output size of POD-RBF models for soil-structure interactions prediction.

Model ID	Quantity	No. of steps	No. of entities	Output size os
1	Settlement $\boldsymbol{S}$	62	2457	152 334
2	Lining moment $\boldsymbol{M}$	62	64 × 76	301 568
3	Lining normal force $\boldsymbol{N}$	62	64 × 76	301 568
4	Lining shear force $\boldsymbol{L}$	62	64 × 76	301 568
5	Lining disp. X $\boldsymbol{u}_x$	62	64 × 76	301 568
6	Lining disp. Y $\boldsymbol{u}_y$	62	64 × 76	301 568
7	Lining disp. Z $\boldsymbol{u}_z$	62	64 × 76	301 568

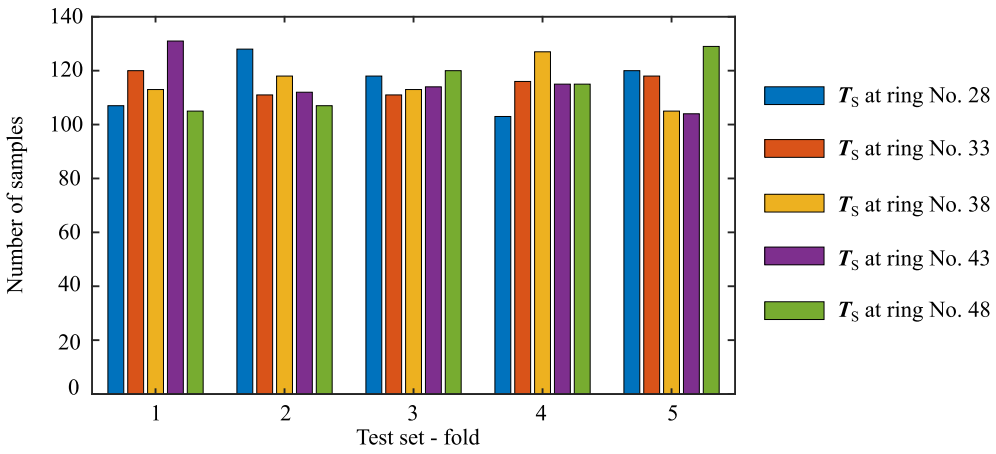

Fig. 10. Data of test set in 5-fold cross-validation for settlement prediction.

Table 4
Prediction performance of 8 POD-RBF surrogate models using 2880 simulations in green field settlement example: L_2 norm error (in (%)) and R^2.

Model ID	Quantity	Error	5-fold cross validation					
			1	2	3	4	5	Avg.
1	Settlement $\boldsymbol{S}$	L_2	1.06	1.08	1.06	1.03	1.02	**1.05**
		R^2	0.999	0.999	0.999	0.999	0.999	**0.999**
2	Lining moment $\boldsymbol{M}$	L_2	1.59	1.60	1.64	1.61	1.66	**1.62**
		R^2	0.999	0.999	0.999	0.999	0.999	**0.999**
3	Lining normal force $\boldsymbol{N}$	L_2	0.94	0.93	0.96	0.94	0.96	**0.95**
		R^2	0.999	0.999	0.999	0.999	0.999	**0.999**
4	Lining shear force $\boldsymbol{L}$	L_2	1.60	1.63	1.66	1.62	1.67	**1.64**
		R^2	0.999	0.999	0.999	0.999	0.999	**0.999**
5	Lining disp. X $\boldsymbol{u}_x$	L_2	1.14	1.14	1.13	1.13	1.17	**1.14**
		R^2	0.999	0.999	0.999	0.999	0.999	**0.999**
6	Lining disp. Y $\boldsymbol{u}_y$	L_2	1.99	2.05	2.00	2.03	1.98	**2.01**
		R^2	0.999	0.999	0.999	0.999	0.999	**0.999**
7	Lining disp. Z $\boldsymbol{u}_z$	L_2	1.27	1.25	1.26	1.27	1.28	**1.27**
		R^2	0.999	0.999	0.999	0.999	0.999	**0.999**

enables a real-time TBM operation support practical application using the proposed surrogate modeling approach.

5.2 TBM process control in urban area with above ground buildings

The simulation model generated in this example represents a tunnel section of a reference project, where the tunnel is excavated underneath an urban area with a large number of buildings. The TBM operation is controlled to minimize the possible damage to existing buildings. Figure 13 depicts the computational domain, the tunnel alignment, the associated buildings, and the section geology. The tunnel has an excavation diameter of 11.34 m with an overburden ranging from 17 to 20 m. The simulated alignment consists of 57 concrete lining rings, each with a length of 2 m and a thickness of 0.4 m. Existing buildings in the investigated area include mainly masonry residential houses, which are typically two to three-story buildings. There are in total 108 buildings taken into consideration in the simulation, however depending on their locations to the tunnel alignment, different LODs are used to model the buildings, see Fig. 13(a). Critical buildings with higher LODs are represented in detail using a structural model with the presence of windows, while less important structures are modeled as connected closed walls and slabs using shell elements.

Figure 13(b) shows the longitudinal ground model of the simulated section, which consists of three soil layers: a top loose sand layer (0S), a medium sand layer (1S), and a dense sand layer (2S). With the assumption that the soil layers are horizontal, the tunnel is thus excavated in the dense sand layer 2S (with a modulus of elasticity $E_{2S} = 66$ MPa) in the first half of the section, while in the rest of the alignment, the tunnel construction is performed in the medium sand layer 1S ($E_{1S} = 37$ MPa). A transition zone of 30 m between two soil layers appears in the area from ring 21 to ring 36, i.e., in the range of 42 to 72 m from the left boundary of the computational domain.

Considering operational parameters, only the face support pressure $\boldsymbol{P}_S$ and the steering time $\boldsymbol{T}_S$ are considered as steering parameters in this example. The grouting pressure is kept correlated with the applied face support pressure following Eq. (9) with $l = 1$. Four steering times

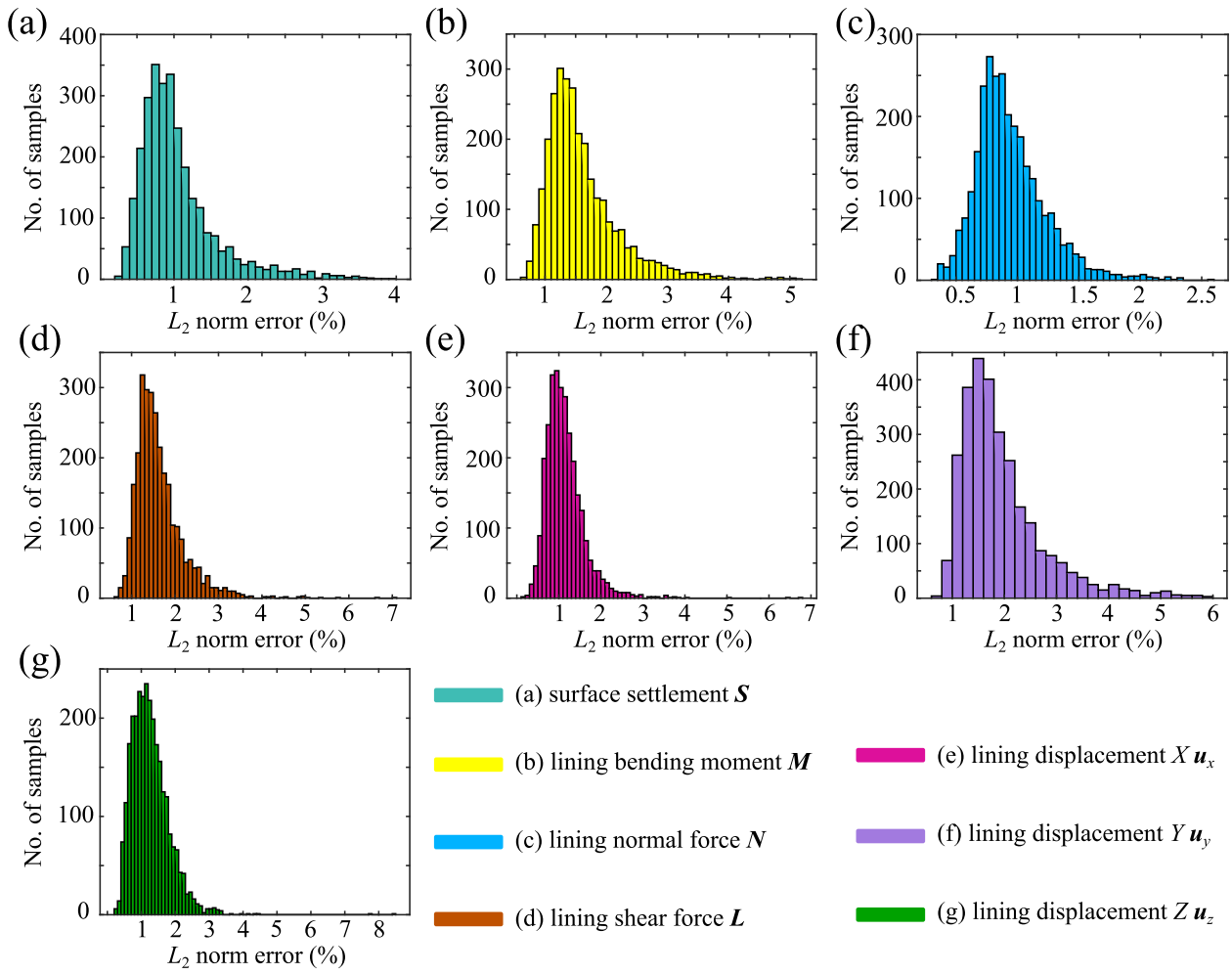

Fig. 11. Surrogate model quality evaluation with histograms of L_2 error distributions.

(at ring 21, ring 26, ring 31, and ring 36) are regarded as input values for the $\boldsymbol{T}_S$ parameter. As compared to the straight tunnel in Section 5.1, the tunnel in this example possesses an inclined alignment, therefore the applied face pressures are required to vary with respect to the depth of the tunnel alignment. By taking the water pressure as a reference, the suggested values for the face pressure $\boldsymbol{P}_S$ are in the range of $[210, 240]$ kPa for the tunnel section. From that reference pressures, nine discretized values in an equivalent distance of the relative change $\Delta\boldsymbol{P}_S$ ($\Delta\boldsymbol{P}_S = [-20 \cdots 60]$ kPa) are designed to form the input discretization of the parameter $\boldsymbol{P}_S$. A combination of possible input values of the two steering parameters $\Delta\boldsymbol{P}_S$ and $\boldsymbol{T}_S$ leads to a total number of 324 input samples (9 samples of $\Delta\boldsymbol{P}_S$ for the left section $\times$ 9 samples of $\Delta\boldsymbol{P}_S$ for the right section $\times$ 4 samples of $\boldsymbol{T}_S$ = 324 input samples). As a result, 324 FC simulations are executed to generate the necessary data for constructing the POD-RBF models.

In this example, the settlements at 931 surface points and the damages on 108 buildings are considered as outputs of the simulations as well as POD-RBF models. It should be noted that in this work, damages are computed and predicted for multiple positions on the buildings. More specifically, each building facade is discretized into a number of frames, where each frame has a certain number of elements. Damages are numerically computed for each element, the average damage value of associated elements in a frame is therefore considered as the damage value of the frame. Overall, there are 698 frames with respect to 108 buildings in the tunnel section. Due to the fact that the damages on buildings depend heavily on the associated surface settlement, a POD-RBF model (Model 8), which considers the operational parameters as inputs, will be firstly set up to predict the settlement at the 931 surface points in all 46 simulation steps. The predicted settlements are then utilized as inputs in another POD-RBF model (Model 9), which is capable to predict the damages on 698 frames of buildings at all 46 steps representing the tunneling process. The output sizes of Model 8 and Model 9 are thus 42 826 and 32 108, respectively.

The damage values can be represented by maximum tensile strains computed directly from FC simulations or by categories of damages (Cod) converted from associated strain values following the commonly used criteria in

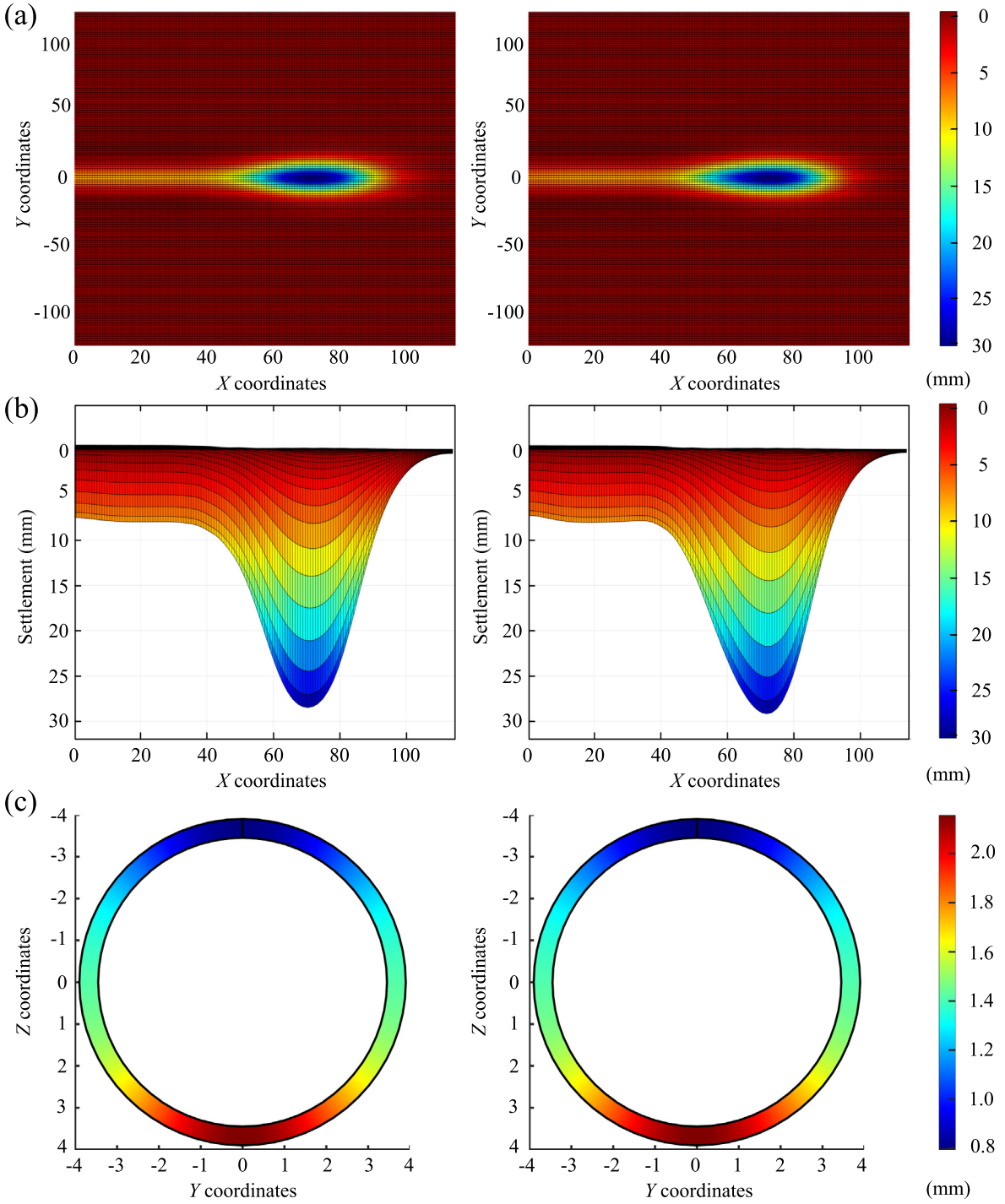

Fig. 12. The test scenarios with worst prediction results (left: reference solutions FC; right: predicted solutions POD-RBF). (a) Surface settlement (top view XY plane), (b) surface settlement (side view XZ plane), and (c) lining deformations $\boldsymbol{u}_z$.

(Boscardin & Cording, 1989), see Fig. 14(b). In practice, the building damage evaluation is usually interpreted with the categories, therefore the POD-RBF models in this example will be tested to predict the tensile strains on multiple positions of buildings. The building damages are then converted to categories and visualized as shown in Fig. 14 (a). Table 5 illustrates the prediction accuracy of POD-RBF models for both surface settlements and tensile strains. Similar to the findings in the green field example in Section 5.1, the settlement prediction from the POD-RBF model shows a great agreement with FC simulation results with a L_2 norm error of only 2.4% and R^2 value of 0.999. In addition, the highly non-linear behavior of strains on buildings can also be well predicted using the POD-RBF method (i.e., the overall L_2 norm error and the R^2 value of 5-fold cross-validation for the strain prediction

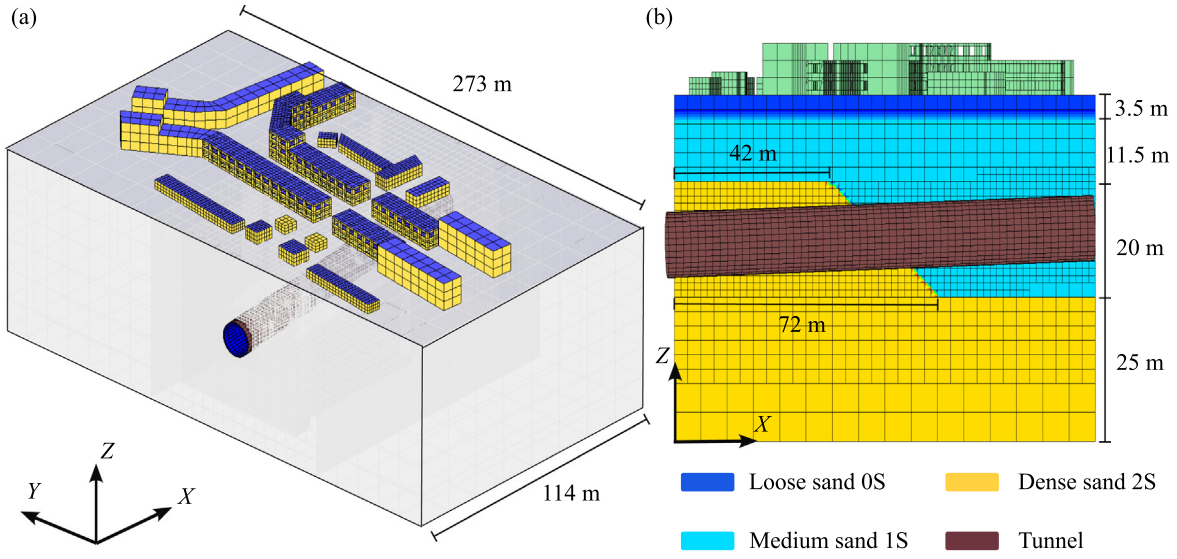

Fig. 13. Simulation model of the tunnel section with buildings. (a) Computational domain with 108 buildings and (b) geological conditions of the simulated section.

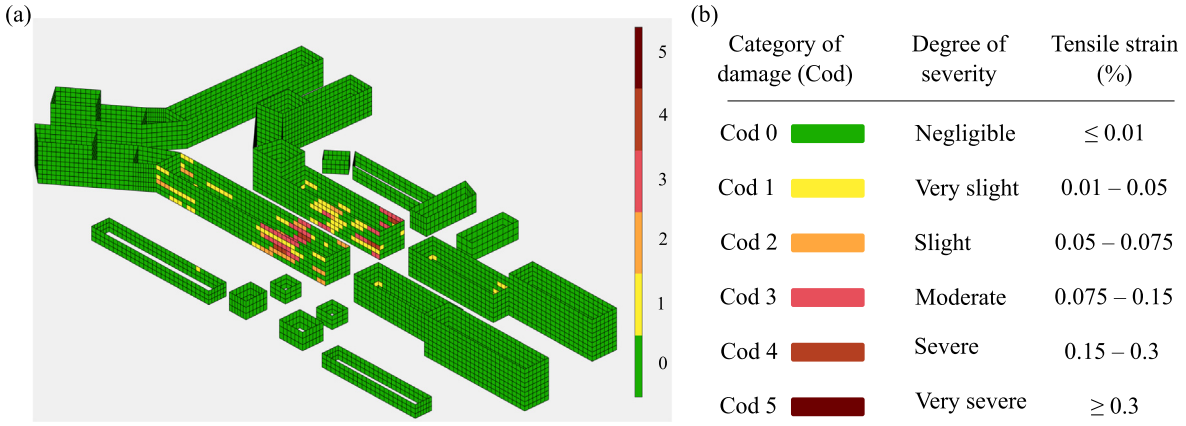

Fig. 14. Building damage evaluation using categories. (a) Visualization of predicted results and (b) damage categories and limiting tensile strains, according to (Boscardin & Cording, 1989).

are 7.52% and 0.996, respectively), while the computation time is substantially reduced from 10 h to only 1 s.

Nevertheless, the quality of category prediction, which contains only discrete values of damage categories, is evaluated based on the confusion matrix. Figure 15 presents the confusion chart of the categories prediction with respect to the 6 damage groups for all 698 frames of the investigated buildings at 46 simulation steps in the 324 testing scenarios. Overall, there are more than ten million predicted values of damage categories (i.e., 698 frames × 46 steps × 324 scenarios = 10 402 992 category values), which will be used to evaluate the prediction quality of the POD-RBF model. From the confusion chart, the true/false predictions of each category can be interpreted intuitively. For example, the "negligible" damage category (i.e., Cod 0) is excellently predicted in 99.9% of the number of

Table 5
Prediction performance of 2 POD-RBF surrogate models using 324 simulations in TBM control example with lots of buildings: L_2 norm error (in (%)) and R^2.

Model ID	Quantity	Error	5-fold cross validation					
			1	2	3	4	5	Avg.
8	Settlement $\boldsymbol{S}$	L_2	2.40	2.39	2.51	2.32	2.39	**2.40**
		R^2	0.999	0.999	0.999	0.999	0.999	**0.999**
9	Tensile strains	L_2	7.40	7.10	7.59	8.10	7.27	**7.52**
		R^2	0.996	0.997	0.996	0.994	0.996	**0.996**

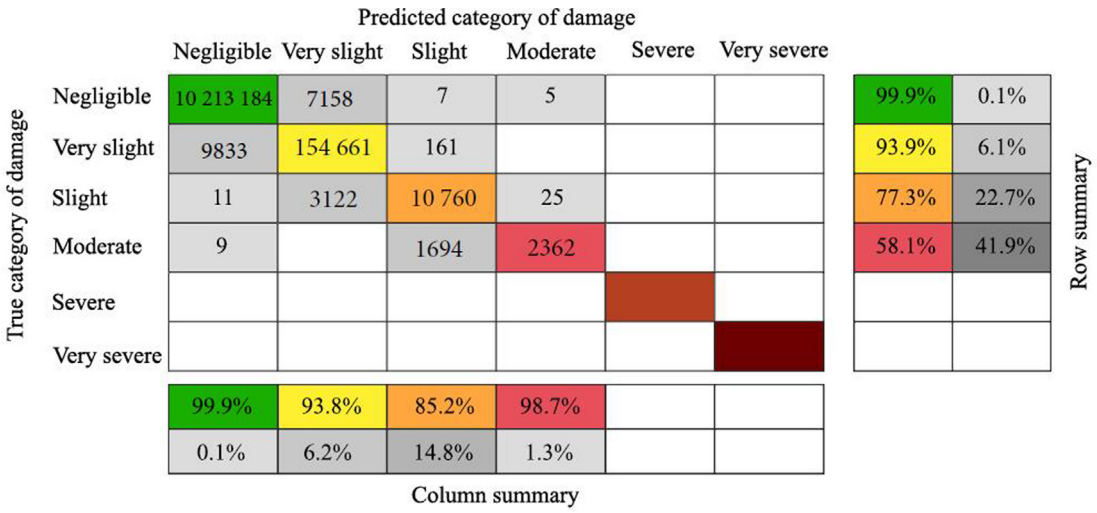

Fig. 15. Confusion matrix of the prediction for categories of damage.

observations. Only 0.1% of the samples (7158 + 7 + 5 = 7170 samples), which are truly characterized with the Cod 0, are predicted to wrong categories (Cod 1 to Cod 5). Similarly, also 0.1% of the samples (9833 + 11 + 9 = 9853 samples), which actually belong to other categories, are wrongly predicted as the Cod 0 with negligible damages. It can be seen that the prediction is also great for other categories except for the case between the Cod 2 and the Cod 3, which is the maximum possible damage category in this example. In this case, 1694 samples, which constitute almost 41.9% of samples with the true label of moderate damages (Cod 3), are inaccurately expected to be in Cod 2 with slight damages. This imprecise prediction of the categories can be explained due to the fact that even a slight false prediction in strain values at the border between Cod 2 and Cod 3 can lead to a wrong estimation in damage categories. However, it can be observed that the misclassification occurs almost only between two consecutive categories of damages, which still shows the reliability of the surrogate model in terms of the prediction for categories of damage. Therefore, considering the high nonlinearities of the example and the accumulated errors from the predicted settlements for the strain prediction, the POD-RBF surrogate models have proven to be able to substitute efficiently the FC simulation model in this example.

6 SMART application development

Based on the described simulation-based strategy, a real-time simulation application called SMART (Simulation-and-Monitoring-based Assistant for Real-time steering in mechanized Tunneling) has been continuously developed with the aim to support the TBM operation during the tunnel construction (Cao et al., 2016, 2018, 2020; Freitag et al., 2018). In this paper, the SMART app has been further supplemented with the possibility to quickly provide not only the surface settlement and the risk of building damages but also structural forces and deformations of the tunnel lining. With respect to each user adjustment of the operational input parameters, the app can provide a complete and quick prediction of all soil-structure interactions in the tunneling process. Depending on expected quantities and desired showing options, outputs can be visualized and presented under different types, such as the time evolution settlement of a monitoring surface point, the 3D surface settlement field at a chosen excavation step, the structural forces and deformations in a lining ring at a specific step. To support the decision-making process, comparisons between multiple investigated scenarios are also made available in SMART. For example, by defining two possible scenarios of operating the TBM, the associated interactions in these scenarios are quickly delivered under different graphs or plots to evaluate the pros and contras for the selected scenarios.

Figure 16 provides a screenshot of the SMART application. On the upper left corner, a graph is designed to show two investigated operation scenarios with given values of process parameters, which are manually adjusted via sliders on the top right corner. An intuitive brief description of the tunnel section, the tunnel geometry, the soil layers, the lining properties, and TBM positions are dynamically visualized in 3D space in the lower left part of the app. Whereas, the lower right area in the window panel is dedicated to the illustration of predicted soil-structure interactions results. Tabs corresponding to main interactions, e.g., the surface settlement and the lining behavior, are available. Depending on the selected types (either evolution or cross section), expected outputs are plotted for a comparison between two selected scenarios, which can suggest an appropriate pressure scenario to ensure possible system responses satisfying a multi-criteria objective.

Figure 17 illustrates an application of SMART for an investigation in the example of TBM process control in an urban area. Two investigated scenarios are depicted in

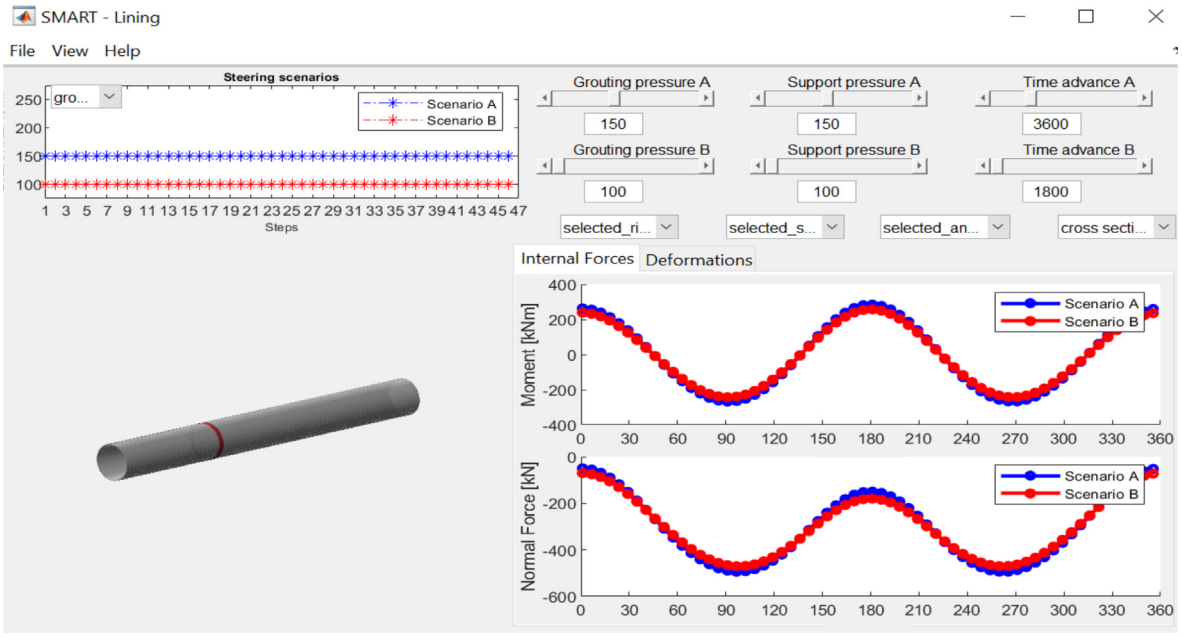

Fig. 16. A screenshot of the SMART application showing the tunnel lining bending moments.

the top left of the panel with the blue line (scenario A) and the red line (scenario B) where the relative change $\Delta \boldsymbol{P}_S$ is kept constant in scenario A and a moderate increase of 40 kPa in $\Delta \boldsymbol{P}_S$ is applied starting from step 26 in scenario B. The resulting damage categories can be observed in two plots at the bottom of the application panel, which shows that the appropriate pressure adjustment in scenario B will lead to a safer situation with lower damage categories in critical buildings in this area, see Fig. 17. Similarly, by changing the sliders of model inputs on the top right panel (i.e., the relative change in support pressure $\Delta \boldsymbol{P}_S$ and the steering moment $\boldsymbol{T}_S$), the associated damages

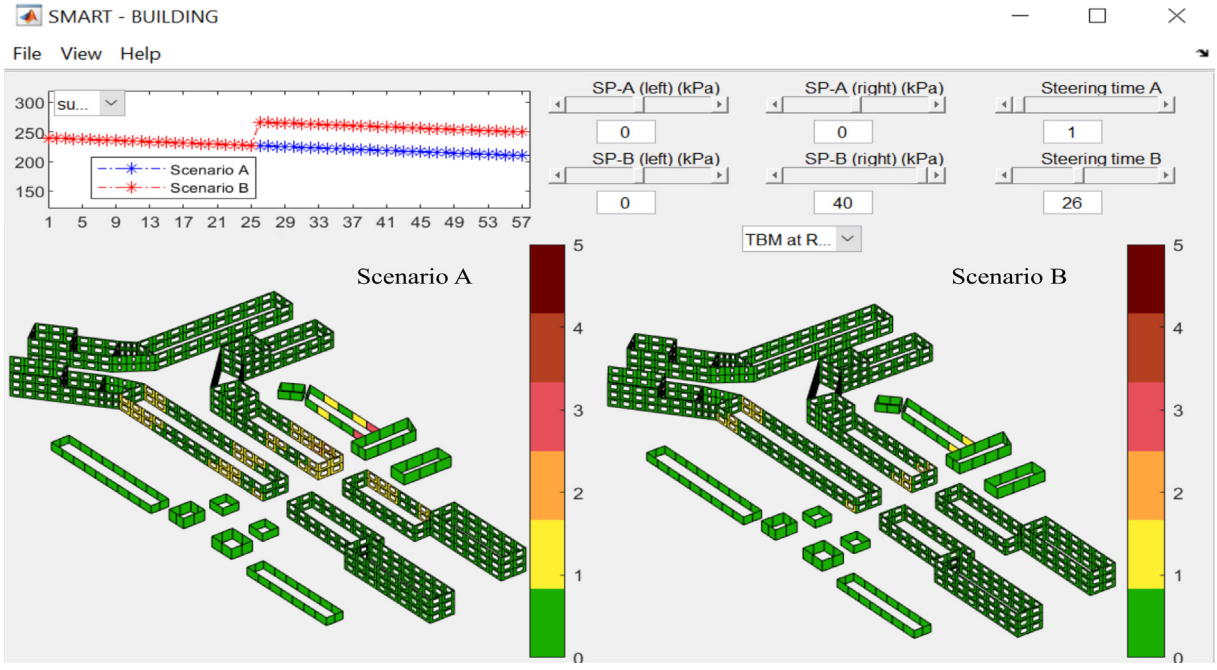

Fig. 17. A screenshot of the SMART application illustrating the usage of damages on buildings to support the selection of face support pressure.

categories in buildings can be quickly computed and visualized, which provides a real-time assistant tool for site engineers to make a decision on how to select the face pressure in next excavation steps.

7 Conclusions

In this paper, the following conclusions can be drawn: (1) In case of a soil layer change, it is very important to adjust and adapt the operational process parameters to account for the expected behavior of the ground ahead. The earlier the soil layer change can be detected and appropriate adjustments are made, the better tunneling-induced effects on the above ground structures can be controlled. As a result, in addition to the face support pressure $\boldsymbol{P}_S$ and the tail void grouting $\boldsymbol{P}_G$, the steering time $\boldsymbol{T}_S$ is also considered as a steering input parameter in the simulation-based TBM operation support strategy; (2) Surrogate models based on the combination of Proper Orthogonal Decomposition and Radial Basis Functions (POD-RBF) are numerically efficient to substitute time-consuming Finite Cell models for the simulation of mechanized tunneling processes. The POD-RBF models have a generalized robust, accurate, and reliable prediction capability. By employing nine POD-RBF models, a huge dimensional output (i.e., approximately two million outputs) of main soil-structure interactions (including surface settlements, risks of damages on buildings, and tunnel lining forces and deformations) can be quickly predicted with similar accuracy as compared to reference solutions from FC simulations. The associated computation time is substantially reduced from 7 to 10 h to only 5 to 10 s; (3) The developed simulation-based SMART application can be used as an assistant system for real-time TBM operation support in practical tunneling.

Currently, the SMART application provides only predicted results, which are available from the FC simulation model. To have better support for tunnel engineers, one possible extension is to integrate multiple sub-models into the SMART application, e.g. a local sub-model for the prediction of tunnel face stability or another sub-model for the prediction of the wear rate of cutting tools. As a result, new operational parameters, e.g., the torque or the rotation speed of the TBM cutter head will be introduced into SMART together with the new soil-structure interactions, which can enhance the support for engineers at tunnel construction sites. Last but not least, the real measurement data will definitely be integrated to update the POD-RBF models during the tunnel construction.

Declaration of competing interest

Günther Meschke is an editorial board member for Underground Space and was not involved in the editorial review or the decision to publish this article. All authors declare that there are no competing interests.

Acknowledgment

Financial support was provided by German Science Foundation (DFG) in the framework of subprojects C1 & T2 of Collaborative Research Center SFB 837 "Interaction Modeling in Mechanized Tunneling" (Project No. 77309832). This support is gratefully acknowledged.

References

Alsahly, A., Stascheit, J., & Meschke, G. (2016). Advanced finite element modeling of excavation and advancement processes in mechanized tunneling. *Advances in Engineering Software, 100*, 198–214.

Bilotta, E., Paolillo, A., Russo, G., & Aversa, S. (2017). Displacements induced by tunnelling under a historical building. *Tunneling and Underground Space Technology, 61*, 221–232.

Boscardin, M., & Cording, E. (1989). Building response to excavation-induced settlement. *ASCE Journal on Geotechnical Engineering, 115*, 1–21.

Buhmann, M. (2003). Radial Basis Functions. *Cam*.

Bui, H. G., & Meschke, G. (2020). A parallelization strategy for hydro-mechanically coupled mechanized tunneling simulations. *Computers and Geotechnics, 120*, 103378.

Bui, H., Cao, B., Freitag, S., Hackl, K., & Meschke, G. (2023). Surrogate modeling for interactive tunnel track design using the cut finite element method. Engineering with Computers.

Bui, H. G., Schillinger, D., Zendaki, Y., & Meschke, G. (2022). A cutfem-based framework for numerical simulations of machine driven tunnels with arbitrary alignments. *Computers and Geotechnics, 144, 104637*.

Bui-Thanh, T., Damodaran, M., & Willcox, K. (2004). Aerodynamic data reconstruction and inverse design using proper orthogonal decomposition. *The American Institute of Aeronautics and Astronautics (AIAA), 42*, 1505–1516.

Cao, B., Freitag, S., & Meschke, G. (2016). A hybrid RNN-GPOD surrogate model for real-time settlement predictions in mechanised tunnelling. *Advanced Modeling and Simulation in Engineering Sciences, 3*(5), 1–22.

Cao, B., Freitag, S., & Meschke, G. (2018). A fuzzy surrogate modelling approach for real-time settlement predictions in mechanised tunnelling. *International Journal of Reliability and Safety, 12*(1/2), 187–217.

Cao, B., Obel, M., Freitag, S., Heußner, L., Meschke, G., & Mark, P. (2022). Real-time risk assessment of tunneling-induced building damage considering polymorphic uncertainty. *ASCE-ASME Journal of Risk and Uncertainty in Engineering Systems, Part A: Civil Engineering, 8*(1), 04021069.

Cao, B., Obel, M., Freitag, S., Mark, P., & Meschke, G. (2020). Artificial neural network surrogate modelling for real-time predictions and control of building damage during mechanised tunnelling. *Advances in Engineering Software*, 149, 102869 (14 pages).

Cao, B., Saadallah, A., Egorov, A., Freitag, S., Meschke, G., & Morik, K. (2021). Online geological anomaly detection using machine learning in mechanized tunneling. In Barla, M., Di Donna, A., and Sterpi, D., editors, *Challenges and Innovations in Geomechanics, Proceedings of the 16th International Conference of IACMAG (IACMAG 2021)*, volume 125 of Lecture Notes in Civil Engineering (pp. 323–330), Turin. Springer Nature Switzerland AG.

Cao, B. T., Heußner, L., Jodehl, A., Obel, M., Salloum, Y., Freitag, S., ... Thewes, M. (2023). *Interaction Modeling in Mechanized Tunneling*, chapter Real-Time Simulation for Steering the Tunnel Construction. In *Process* (pp. 405–463). Switzerland, Cham: Springer Nature.

Cheng, P., Liu, F., Xu, Y., & Li, Y. (2023). Regulating bulkhead pressure of epb shield machines through dem modeling and data mining. *Underground Space, 8*, 15–29.

Do, N. A., Dias, D., Golpasand, M.-R. B., Dang, V. K., Nait-Rabah, O., Pham, V. V., & Dang, T. T. (2022). Numerical analyses of twin stacked

mechanized tunnels in soft grounds - influence of their position and construction procedure. *Tunneling and Underground Space Technology, 130*, 104734.
Do, N.-A., Dias, D., Oreste, P., & Djeran-Maigre, I. (2014). Three-dimensional numerical simulation of a mechanized twin tunnels in soft ground. *Tunnelling and Underground Space Technology, 42*(40–51), 00052.
Everson, R., & Sivorich, L. (1995). Karhunen-loeve procedure for gappy data. *Journal of the Optical Society of America A: Optics, Image Science and Vision, 12*(8), 1657–1664.
Fargnoli, V., Boldini, D., & Amorosi, A. (2015). Twin tunnel excavation in coarse grained soils: Observations and numerical back-predictions under free field conditions and in presence of a surface structure. *Tunneling and Underground Space Technology, 49*, 454–469.
Freitag, S., Cao, B., Ninic, J., & Meschke, G. (2018). Recurrent neural networks and proper orthogonal decomposition with interval data for real-time predictions of mechanised tunnelling processes. *Computers and Structures*, 207, 258–273.
Freitag, S., Cao, B. T., Ninić, J., & Meschke, G. (2015). Hybrid surrogate modelling for mechanised tunnelling simulations with uncertain data. *International Journal of Reliability and Safety, 9*(2/3), 154–173.
Gan, X., Yu, J., Gong, X., & Zhu, M. (2022). Probabilistic analysis for twin tunneling-induced longitudinal responses of existing shield tunnel. *Tunneling and Underground Space Technology, 120*, 104317.
German Tunnelling Committee (DAUB) (2000). Recommendations for design and operation of shield machines. Technical report, Deutscher Ausschuss für unterirdisches Bauen e. V. (DAUB).
German Tunnelling Committee (DAUB) (2016). Recommendations for face support pressure calculations for shield tunnelling in soft ground. Technical report, Deutscher Ausschuss für unterirdisches Bauen e. V. (DAUB).
Gong, C., Ding, W., & Xie, D. (2020). Twin epb tunneling-induced deformation and assessment of a historical masonry building on shanghai soft clay. *Tunneling and Underground Space Technology, 98*, 103300.
Guo, C., Guo, Q., Zhang, T., Li, W., Zhu, H., & Yan, Z. (2022). Study on real-time heat release rate inversion for dynamic reconstruction and visualization of tunnel fire scenarios. *Tunneling and Underground Space Technology, 122*, 104333.
Hardy, R. (1990). Theory and applications of the multiquadric-biharmonic method: 20 years of discovery 1968–1988. *Computers & Mathematics with Applications, 19*(8–9), 163–208.
He, L., Liu, Y., Bi, S., Wang, L., Broggi, M., & Beer, M. (2020). Estimation of failure probability in braced excavation using bayesian networks with integrated model updating. *Underground Space, 5*(4), 315–323.
Kavvadas, M., Litsas, D., Vazaios, I., & Fortsakis, P. (2017). Development of a 3d finite element model for shield epb tunnelling. *Tunneling and Underground Space Technology, 65*, 22–34.
Khaledi, K., Miro, S., König, M., & Schanz, T. (2014). Robust and reliable metamodels for mechanized tunnel simulations. *Computers and Geotechnics, 61*, 1–12.
Lai, J., Zhou, H., Wang, K., Qiu, J., Wang, L., Wang, J., & Feng, Z. (2020). Shield-driven induced ground surface and ming dynasty city wall settlement of xián metro. *Tunneling and Underground Space Technology, 97*, 103220.
Li, C., Zhou, J., Armaghani, D. J., & Li, X. (2021). Stability analysis of underground mine hard rock pillars via combination of finite difference methods, neural networks, and monte carlo simulation techniques. *Underground Space, 6*(4), 379–395.
Lü, Q., Xiao, Z.-P., Ji, J., & Zheng, J. (2017). Reliability based design optimization for a rock tunnel support system with multiple failure modes using response surface method. *Tunneling and Underground Space Technology, 70*, 1–10.
Maidl, B., Herrenknecht, M., Maidl, U., & Wehrmeyer, G. (2012). *Mechanised shield tunnelling*. Ernst und Sohn.
Majumder, D., Chakraborty, S., & Chowdhury, R. (2017). Probabilistic analysis of tunnels: A hybrid polynomial correlated function expansion based approach. *Tunneling and Underground Space Technology, 70*, 89–104.
Marwan, A., Gall, V., Alsahly, A., & Meschke, G. (2021). Structural forces in segmental linings: Process-oriented tunnel advance simulations vs. conventional structural analysis. Tunneling and Underground. *Space Technology, 111*(103836).
Meschke, G. (1996). Consideration of aging of shotcrete in the context of a 3D viscoplastic material model. *International Journal for Numerical Methods in Engineering, 39*, 3123–3143.
Meschke, G., Freitag, S., Ninić, J., and Cao, B. (2013). Simulations- und monitoring-basierte prozesssteuerung im maschinellen tunnelbau. In Kaliske, M. and Graf, W., editors, *Ingenieurwissen und Vorschriftenwerk, 17. Dresdner Baustatik-Seminar* (pp. 127–149). Institut für Statik und Dynamik der Tragwerke, TU Dresden.
Miliziano, S., & de Lillis, A. (2019). Predicted and observed settlements induced by the mechanized tunnel excavation of metro line c near s. giovanni station in rome. *Tunneling and Underground Space Technology, 86*, 236–246.
Namazi, E., Mohamad, H., & Hajihassani, M. (2021). 3d behaviour of buildings due to tunnel induced ground movement. *Transportation Geotechnics, 31*, 100661.
Ni, P., & Mangalathu, S. (2018). Fragility analysis of gray iron pipelines subjected to tunneling induced ground settlement. *Tunneling and Underground Space Technology, 76*, 133–144.
Ninić, J., Bui, H. G., Koch, C., & Meschke, G. (2019). Computationally efficient simulation in urban mechanized tunneling based on multilevel bim models. *Journal of Computing in Civil Engineering, 33*(3), 04019007.
Ninić, J., Freitag, S., & Meschke, G. (2017). A hybrid finite element and surrogate modelling approach for simulation and monitoring supported TBM steering. *Tunnelling and Underground Space Technology, 63*, 12–28.
Ninić, J., & Meschke, G. (2015). Model update and real-time steering of tunnel boring machines using simulation-based meta models. *Tunnelling and Underground Space Technology, 45*, 138–152.
Ninić, J., & Meschke, G. (2017). Simulation based evaluation of time-variant loadings acting on tunnel linings during mechanized tunnel construction. *Engineering Structures, 135*, 21–40.
Ochmanski, M., Modoni, G., & Bzowka, J. (2018). Automated numerical modelling for the control of epb technology. *Tunneling and Underground Space Technology, 75*, 117–128.
Radermacher, A., & Reese, S. (2014). Model reduction in elastoplasticity: Proper orthogonal decomposition combined with adaptive substructuring. *Computational Mechanics, 54*(3), 677–687.
Selby, A. (1999). Tunnelling in soils - ground movements, and damage to buildings in workington, uk. *Geotechnical and Geological Engineering, 17*, 351–371.
Smith, T., Moehlis, J., & Holmes, P. (2005). Low-dimensional modelling of turbulence using proper orthogonal decomposition: A tutorial. *Nonlinear Dynamics, 41*, 275–307.
Suwansawat, S., & Einstein, H. H. (2006). Artificial neural networks for predicting the maximum surface settlement caused by epb shield tunneling. *Tunnelling and Underground Space Technology, 21*(2), 133–150.
Tao, Y., He, W., Sun, H., Cai, Y., & Chen, J. (2022). Multi-objective optimization-based prediction of excavation-induced tunnel displacement. *Underground Space, 7*(5), 735–747.
Wang, Q., Fang, H., & Shen, L. (2016). Reliability analysis of tunnels using a metamodeling technique based on augmented radial basis functions. *Tunneling and Underground Space Technology, 56*, 45–53.
Xie, X., Yang, Y., & Ji, M. (2016). Analysis of ground surface settlement induced by the construction of a large-diameter shield-driven tunnel in shanghai, china. *Tunneling and Underground Space Technology, 51*, 120–132.
Zendaki, Y., Cao, B., Alsahly, A., Freitag, S., and Meschke, G. (2022). Simulation-based surrogate models for real-time tunnel lining behavior predictions. In *International Conference on Computational Methods and Information Models in Tunneling (EURO:TUN)*, Bochum, Germany.
Zendaki, Y., & Meschke, G. (2022). Adaptive mesh refinement using octree for finite cell simulation and its application for tunneling in saturated soils. *PAMM, 22*(S4).
Zhang, W., Li, Y., Wu, C., Li, H., Goh, A., & Liu, H. (2022). Prediction of lining response for twin tunnels constructed in anisotropic clay using machine learning techniques. *Underground Space, 7*(1), 122–133.
Zhang, W., Zhang, R., Wu, C., Goh, A. T., & Wang, L. (2020). Assessment of basal heave stability for braced excavations in anisotropic clay using extreme gradient boosting and random forest regression. *Underground Space, 7*(2), 233–241.

Zhao, C., Lavasan, A., Barciaga, T., Kämper, C., Mark, P., & Schanz, T. (2017). Prediction of tunnel lining forces and deformations using analytical and numerical solutions. *Tunneling and Underground Space Technology, 64*, 164–176.

Zhao, T., Han, T., Wu, G., Gao, Y., & Lu, Y. (2021). Effects of grouting in reducing excessive tunnel lining deformation: Field experiment and numerical modelling using material point method. *Tunneling and Underground Space Technology, 116*, 104114.

Zheng, G., Fan, Q., Zhang, T., & Zhang, Q. (2022). Numerical study of the soil-tunnel and tunnel-tunnel interactions of epbm overlapping tunnels constructed in soft ground. *Tunneling and Underground Space Technology, 124*, 104490.

Zheng, H., Mooney, M., & Gutierrez, M. (2023). Surrogate model for 3d ground and structural deformations in tunneling by the sequential excavation method. *Computers and Geotechnics, 154*, 105142.

Zhu, C., Wang, S., Peng, S., & Song, Y. (2022). Surface settlement in saturated loess stratum during shield construction: Numerical modeling and sensitivity analysis. *Tunneling and Underground Space Technology, 119*, 104205.

Zhuang, D., Ma, K., Tang, C., Liang, Z., Wang, K., & Wang, Z. (2019). Mechanical parameter inversion in tunnel engineering using support vector regression optimized by multi-strategy artificial fish swarm algorithm. *Tunneling and Underground Space Technology, 83*, 425–436.